ABSTRACT

Title of Document: Novel Integrated System Architecture for an Autonomous Jumping Micro-Robot

Wayne A. Churaman, M.S., 2010

Directed By: Dr. Neil Goldsman, ECE ; Dr. Sarah Bergbreiter, ME

As the capability and complexity of robotic platforms continue to evolve from the macro to micro-scale, innovation of such systems is driven by the notion that a robot must be able to sense, think, and act [1]. The traditional architecture of a robotic platform consists of a structural layer upon which, actuators, controls, power, and communication modules are integrated for optimal system performance. The structural layer, for many micro-scale platforms, has commonly been implemented using a silicon die, thus leading to robotic platforms referred to as "walking chips" [2]. In this thesis, the first-ever jumping microrobotic platform is demonstrated using a hybrid integration approach to assemble on-board sensing and power directly onto a polymer chassis. The microrobot detects a change in light intensity and ignites 0.21mg of integrated nanoporous energetic silicon, resulting in 246μJ of kinetic energy and a vertical jump height of 8cm.

Report Documentation Page

Form Approved
OMB No. 0704-0188

Public reporting burden for the collection of information is estimated to average 1 hour per response, including the time for reviewing instructions, searching existing data sources, gathering and maintaining the data needed, and completing and reviewing the collection of information Send comments regarding this burden estimate or any other aspect of this collection of information, including suggestions for reducing this burden, to Washington Headquarters Services, Directorate for Information Operations and Reports, 1215 Jefferson Davis Highway, Suite 1204, Arlington VA 22202-4302 Respondents should be aware that notwithstanding any other provision of law, no person shall be subject to a penalty for failing to comply with a collection of information if it does not display a currently valid OMB control number

1. REPORT DATE **2010**	2. REPORT TYPE	3. DATES COVERED **00-00-2010 to 00-00-2010**
4. TITLE AND SUBTITLE **Novel Integrated System Architecture for an Autonomous Jumping Micro-Robot**		5a. CONTRACT NUMBER 5b. GRANT NUMBER 5c. PROGRAM ELEMENT NUMBER
6. AUTHOR(S)		5d. PROJECT NUMBER 5e. TASK NUMBER 5f. WORK UNIT NUMBER
7. PERFORMING ORGANIZATION NAME(S) AND ADDRESS(ES) **University of Maryland, College Park,College Park,MD,20742**		8. PERFORMING ORGANIZATION REPORT NUMBER
9. SPONSORING/MONITORING AGENCY NAME(S) AND ADDRESS(ES)		10. SPONSOR/MONITOR'S ACRONYM(S) 11. SPONSOR/MONITOR'S REPORT NUMBER(S)

12. DISTRIBUTION/AVAILABILITY STATEMENT
Approved for public release; distribution unlimited

13. SUPPLEMENTARY NOTES

14. ABSTRACT

As the capability and complexity of robotic platforms continue to evolve from the macro to micro-scale, innovation of such systems is driven by the notion that a robot must be able to sense, think, and act [1]. The traditional architecture of a robotic platform consists of a structural layer upon which, actuators, controls, power, and communication modules are integrated for optimal system performance. The structural layer, for many micro-scale platforms, has commonly been implemented using a silicon die, thus leading to robotic platforms referred to as ???walking chips??? [2]. In this thesis, the first-ever jumping microrobotic platform is demonstrated using a hybrid integration approach to assemble on-board sensing and power directly onto a polymer chassis. The microrobot detects a change in light intensity and ignites 0.21mg of integrated nanoporous energetic silicon, resulting in 246??J of kinetic energy and a vertical jump height of 8cm.

15. SUBJECT TERMS

16. SECURITY CLASSIFICATION OF:			17. LIMITATION OF ABSTRACT	18. NUMBER OF PAGES	19a. NAME OF RESPONSIBLE PERSON
a REPORT **unclassified**	b ABSTRACT **unclassified**	c THIS PAGE **unclassified**	**Same as Report (SAR)**	**94**	

Standard Form 298 (Rev. 8-98)
Prescribed by ANSI Std Z39-18

Novel Integrated System Architecture for an Autonomous Jumping Micro-Robot

By

Wayne A. Churaman

Thesis submitted to the Faculty of the Graduate School of the
University of Maryland, College Park, in partial fulfillment
of the requirements for the degree of

Master's of Science in
Electrical Engineering
2010

Advisory Committee:
Dr. Neil Goldsman, Chair
Dr. Sarah Bergbreiter
Dr. Martin Peckerar

© Copyright by
Wayne A. Churaman
2010

Dedication

To my beautiful wife,
Gelen, for her tremendous love and support
in making this dream a reality.
Thank you for believing in me
and for encouraging me to strive for the best.
I love you.

To my parents and little sister,
Walter, Sandra, and Maria,
for believing in me,
and for always praying for me.

Acknowledgements

My colleagues and management at the U.S. Army Research Laboratory
for providing me the opportunity to expand my horizons.

The Micro Robotics Lab at the University of Maryland
and Ms. Jessica Rajkowski.

Dr. Sarah Bergbreiter, Dr. Neil Goldsman, and Dr. Martin Peckerar.

Table of Contents

Dedication……ii
Acknowledgements……..iii
Table of Contents……..iv
List of Tables……....vi
List of Figures……..vii

Chapter 1: Introduction…… 1
Section 1.1: Design Challenges…….....1
Section 1.1.1: Locomotion……1
Section 1.1.2: Integration……...2
Section 1.2: Previous Work on Macro-Scale Robots……4
Section 1.2.1: Summary of Macro-Scale Robots……..9
Section 1.3: Previous Work on Micro-Scale Robots……....9
Section 1.3.1: Centimeter Scale Micro Robots……10
Section 1.3.2: Sub-Centimeter Scale Micro Robots……13
Section 1.3.3: Summary of Micro-Scale Robots……16

Chapter 2: Physics of Jumping……17
Section 2.1: Biological Motivation……..17
Section 2.2: Jumping Dynamics……..18

Chapter 3: Actuator Design……21
Section 3.1: Introduction to Actuators……21
Section 3.2: Mechanical Actuators for Jumping Robots……22
Section 3.3: Chemical Actuators for Jumping Robots……25
Section 3.4: Porous Silicon as an Actuator……28
Section 3.4.1: Overview……..30
Section 3.4.2: Actuation using Energetic Nanoporous Silicon……...30
Section 3.4.3: Actuation Requirements……...33

Chapter 4: Sensor and Control……36
Section 4.1: Circuit Design……36
Section 4.2: Capacitor Switch Test……37
Section 4.3: Large Scale Circuit Prototype……40
Section 4.3.1: Large Scale Circuit Operation……41
Section 4.4: Miniaturized Circuit……42
Section 4.4.1: Miniaturized Circuit Operation……43
Section 4.5: Cadence Model…… 44

Chapter 5: Integration……49
Section 5.1: Integration on Silicon…… 50

Section 5.1.1: Hybrid Integration on Silicon Substrate……50
Section 5.1.2: Circuit Assembly on Silicon Substrate……. 51
Section 5.2: Integration on Polymer…… 54
Section 5.2.1: Hybrid Integration on Flexible Substrate……. 55
Section 5.2.2: Circuit Assembly on Flexible Substrate……... 57
Section 5.3: Integration of Nanoporous Energetic Si……61

Chapter 6: Experimentation……..65
Section 6.1: Electrical Characterization…… 65
Section 6.2: Jumping Micro Robot…….. 67
Section 6.2.1: Hybrid Integration on Silicon……... 67
Section 6.2.2: Hybrid Integration on Flexible Substrate……..69

Chapter 7: Conclusions and Future Work……74
Section 7.1: Conclusions…….. 74
Section 7.2: Future Work……. 75

List of Tables

Table 1 Summary of five macro-scale robots comparing size, weight, and actuator used to achieve locomotion

Table 2 Summary of design and operation specifications for centimeter scale platforms

Table 3 Summary of design and operation specifications for sub-centimeter platforms

Table 4 Mass comparison of components needed to construct the RoACH

Table 5 The effect of drag and take-off velocity on jump height and distance

Table 6 Summary of actuation implemented by several jumping robots

Table 7 Comparison of nanoporous energetic silicon with nanothermites

Table 8 System requirements for nanoporous energetic silicon

Table 9 Mass of individual components used to assemble hexapod on silicon

Table 10 Mass of individual components used to assemble hexapod on polymer chassis

List of Figures

Figure 1 Computer model of jumping microrobot showing 1) polymer chassis, 2) nanoporous energetic Si thruster, and 3) control circuit

Figure 2 The Mini-Whegs 9J robot is capable of running and jumping locomotion

Figure 3 Leg-in-Rotor rescue robot uses pneumatic actuators to jump over debris

Figure 4 Electrical and mechanical components used to design the Leg-in-Rotor robot

Figure 5 Scout robot where the spring foot is located to the rear

Figure 6 Integrated electrical system with mechanical assembly for hopping robot

Figure 7 Piston of Sandia Hopper actuated through combustion of propane

Figure 8 The RoACH robot size comparison to U.S. quarter

Figure 9 Jumping robot capable of jumping 1.4m in height

Figure 10 Scratch drive actuator and cantilever steering arm is used to maneuver the robot

Figure 11 Conceptual image of I-SWARM robot

Figure 12 Silicon microrobot with polyimide joint actuators

Figure 13 Images of leafhopper Cicadella Viridis hopping showing (A) lateral view and (B) ventral view

Figure 14 Spring loaded mechanism used to actuate legs with eccentric cam used to store energy

Figure 15 7g jumping robot uses elastic elements in legs to jump up to 1.4m

Figure 16 Braided pnuematic actuator used to drive microrobot joints

Figure 17 Robot legs held in place by electrostatic clamps

Figure 18 Digital propulsion microthruster chip

Figure 19 MEMS silicon microthruster designed with to ignite solid propellant

Figure 20 (A) Top down view of nanoporous silicon before application of oxidizer (B) Ignition of 1cm diameter nanoporous energetic silicon sample with spark

Figure 21 Four individually addressable 2mm nanoporous energetic Si devices

Figure 22 Thrust demonstrated to propel an aluminum foil flyer

Figure 23 Jump trajectory for a 314mg hexapod modeled using MATLAB

Figure 24 Switching circuit used to charge and discharge a capacitor to ignite actuator

Figure 25 Discharge of 10μF capacitor through 3Ω resistor using the simplified switching circuit

Figure 26 Electrical response of thermal initiator used to actuate energetic

Figure 27 Schematic of circuit with light sensor used to detect and thermally ignite porous silicon.

Figure 28 Discharge current through resistor when capacitor charged to 5V

Figure 29 Miniature circuit with sensing and actuation capability

Figure 30 Circuit modeled in Cadence

Figure 31 Current as light is shown onto the circuit

Figure 32 Current level when no light is detected by the circuit

Figure 33 100μF capacitor discharge time in dark condition

Figure 34 Au electrical traces lithographically patterned on silicon nitride

Figure 35 Process flow used to pattern and coat binding sites

Figure 36 Circuit assembled on Si substrate

Figure 37 Light detector circuit located on top side of hexapod

Figure 38 Porous silicon located underneath hexapod

Figure 39 Hexapod made from Loctite polymer

Figure 40 Micro-gripper made from Loctite and actuated with SMA

Figure 41 Hexapod with evaporated Cu traces

Figure 42 Surface mount resistors attached to hexapod chassis using low temperature alloy

Figure 43 (A) Circuit attached directly to hexapod chassis (B) Delamination of metal traces when polymer flexed

Figure 44 Cracking in metal electrical traces

Figure 45 Solder joints made directly to FET and capacitor before assembling circuit on hexapod

Figure 46 Metal pads attached to energetic chip using Loctite

Figure 47 Circuit connected to oxidized nanoporous Si by soldering to pads on the substrate

Figure 48 Capacitor discharge voltage as a function of time

Figure 49 Current across initiator after capacitor is charged for 8 minutes

Figure 50 Circuit assembled on Si substrate and connected to nanoporous silicon

Figure 51 Successive frames showing 6cm jump of hexapod with circuit assembled on Si substrate

Figure 52 Successive frames showing 8cm jump of hexapod with circuit assembled on polymer chassis

Chapter 1: Introduction

1.1 Design Challenges

Robotic platforms, whether designed on a macro or micron scale, require essential components including sensors, actuators, electronic circuits, and a power source to be deemed truly autonomous [3]. The complexity and implementation of these components may vary depending on the application space. These may range from planetary exploration using a hopping robot as proposed in [4], to a system whose task is to serve as a "jumping and rolling inspector" to search out victims under the rubble of a collapsed building [5]. The size of the design platform dictates the unique challenges associated with the type of locomotion, actuation, and system integration, each of which must be addressed when designing a robot.

1.1.1 Locomotion

Robot locomotion refers to how "robot appendages and control mechanisms" can be designed for more efficient movement [6]. The most common types of locomotion include: walking, running, rolling, hopping, and crawling. The type of actuator used to achieve locomotion can include: electrostatic, thermal, shape memory alloy (SMA), piezoelectric, magnetic, etc. Each actuator has a unique set of characteristics, which include operating voltage, achievable displacement, force, speed, compactness, and the type of motion. These characteristics must be considered when designing a robot to maneuver in a particular operating environment.

Where flat, unobstructed surfaces are representative of the terrain to be traversed, walking locomotion demonstrated in [7] may be suitable. As the operating environment changes, the type of locomotion must be chosen to meet the functional needs of the robotic platform. For the mountainous regions of Afghanistan, where centimeter scale rocks and boulders must be traversed, jumping locomotion offers an effective solution to ensuring mobility. For each of these platforms, the power needed to actuate and provide sensing must be integrated on a single platform for true autonomy.

1.1.2 Integration

System integration on the robot requires control circuits which provide the necessary actuation commands, while manipulating sensor data in a continuous feedback loop to make decisions concerning the appropriate actions that should be taken. These systems can be implemented on a macro scale using Commercial Off-The-Shelf (COTS) electronics. As the design platform decreases in size to a few square millimeters, the ability to embed this level of functionality becomes a unique challenge [3]. For millimeter-scale robotic platforms, implementation of electronic circuits has been achieved using Application Specific Integrated Circuits (ASICs) to reduce the chip area. The main drawback with ASICs is that the circuits must be designed from the ground-up, therefore resulting in slower manufacturing turn-around time and higher costs. While the assembly of COTS on PCB is a viable integration approach for large scale robotic platforms, alternative techniques must be developed to provide complex functionality on the sub-centimeter and micron scale.

This thesis describes the first autonomous jumping microrobot, which is fabricated using a polymer integration technique, where the electronic control circuit is assembled and integrated directly onto the chassis of the robot. The integrated circuit provides on-board sensing, enabling the robot to jump in response to a change in light intensity, allowing it to maneuver over centimeter size obstacles. The robot in this work is referred to as a "microrobot" because fabrication requires patterning micron scale features on the polymer chassis. Integration of the circuit is demonstrated using a low temperature solder dipping process, where both the polymer substrate and surface mount components are dipped and then assembled on a hotplate. Figure 1 shows a computer modeled rendering of the microrobot, with 1) a polymer chassis, 2) nanoporous energetic silicon thruster, and 3) control circuit which includes a light sensor and power supply.

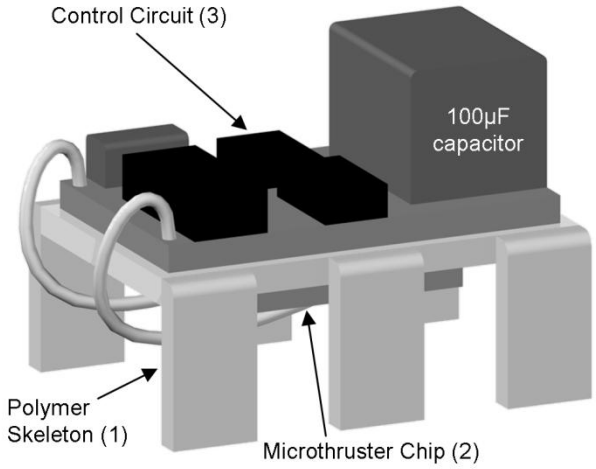

Figure 1 Computer model of jumping microrobot showing 1) polymer chassis, 2) nanoporous energetic Si thruster, and 3) control circuit

While jumping locomotion in robotic platforms has been demonstrated with spring mechanisms and pneumatic actuators as discusses in Chapter 3, this work

provides an alternative to achieve jumping using a high energy density energetic material to actuate the microrobot. The novel nano-scale energetic material, which acts as a propellant, generates thrust in the upward direction serving as a propulsion mechanism. The mechanics of jumping locomotion will be examined in Chapter 2.

1.2 Previous Work on Macro-scale Robots

Macro-scale robots have the advantage of sustaining relatively large payload, which provides added functionality, ranging from data acquisition to on-board communication. Additional space on the chassis provides a platform for supplying power to achieve such operation. These enabling features, allow the platform to act in environments requiring minimal human intervention. Although there exists an inherent inability to explore small spaces, a unique level of interaction must take place between system components to accomplish a desired task. Table 1 summarizes five macro-scale robots, each with the ability to achieve jumping locomotion.

Robot	Size	Locomotion	Actuation	Weight
Mini-Whegs [8]	10.4cm length	Run, Jump	Motor, spring	191.4g
Leg-in-Rotor [5]	300mm x 300mm	Roll, Jump	Pneumatic	<2kg
Scout [9]	40mm dia., 115mm length	Roll, Jump	Servo, spring	200g
Hopping Robot [4]	tens of centimeters	Jump	Motor, spring	450kg
Sandia [10]	0.1m x 0.1m x 0.2m	Jump	Chemical	2.5kg

Table 1 Summary of five macro-scale robots comparing size, weight, and actuator used to achieve locomotion.

The Mini-Whegs Robot

The Mini-Whegs 9J in Figure 2 is a 10.4 cm long robot capable of running and jumping using a single propulsion motor drive train and steering components,

which interface with an on-board radio control unit. Assembly of this system is achieved using an upper and lower shell made from Delrin® that is held together by a set of four nylon screws. The components are positioned vertically beneath the shell, and held in place by short internal walls [8]. The robot requires manual assembly and uses COTS components for actuation.

Figure 2 The Mini-Whegs 9J is capable of running and jumping locomotion [8]

Leg in Rotor Jumping Inspector

With the ability to seek out and find, the Leg-in-Rotor Jumping Inspector shown in Figure 3, is designed to jump over obstacles measuring 60cm to 1m in height [5]. While this can be demonstrated without the implementation of posture-stabilizing controls, it requires the integration of a pneumatic mechanical actuator system connected to an on-board camera that displays information to the outside world. Figure 4 shows the basic system for the Leg-in-Rotor II, consisting of two wheels and a pneumatic cylinder, along with an RC servo motor and DC motor.

Figure 3 Leg-in-Rotor rescue robot uses pneumatic actuators to jump over debris [5]

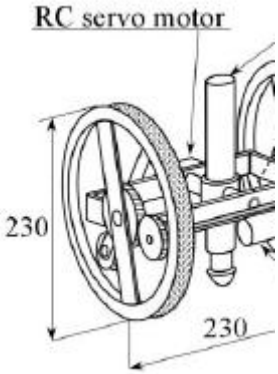

Figure 4 Electrical and mechanical components used to design the Leg-in-Rotor robot

The Scout Robot

For many robotic platforms, the complexity of the system depends on the application space. A key application is deployment in search and rescue operations that require the system to acquire and interpret information for fast, efficient response. The Scout Robot designed by the Center for Distributed Robotics at the University of Minnesota relies on a fully integrated system, which includes microcontrollers, transmitters, magnetometers, tiltometers, shaft encoders, and video camera [9]. The software architecture allows for a larger robot, known as a Ranger robot, to accompany up to 10 Scouts, while using an on-board computer to coordinate

and relay information amongst the Scouts. The integration scheme used to develop this system requires the assembly of COTS circuits and software to aid in teleoperation of the Scout.

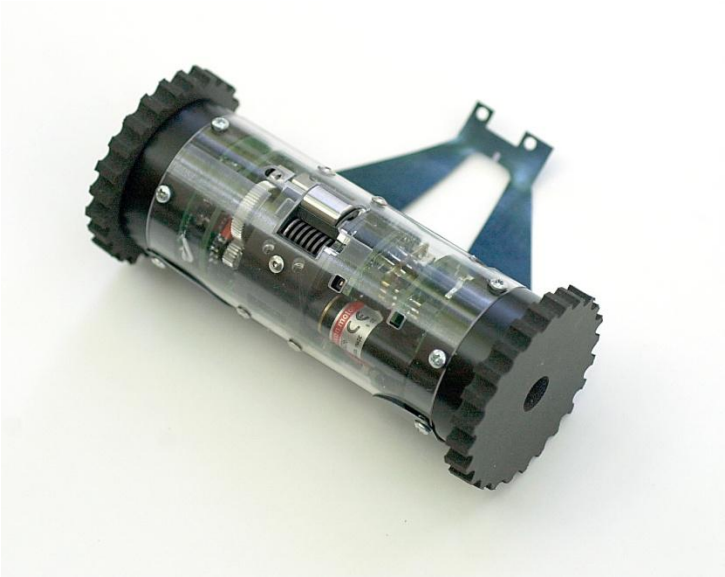

Figure 5 Scout robot similar to that shown in [9] where the spring foot is located to the rear [11].

Hopping Robot for Planetary Exploration

The mechanism for a hopping robot in Figure 6 is a fully integrated system composed of electronic control boards, spring housing, and camera and transmitter assembly. Integration of this system involves an assembled external shell comprised of a motor support fixed to the upper shell, along with a base plate fixed to the lower shell. Two cylinders for the spring housing are used, where fixed pins attached to the internal cylinder allow it to slide into grooves located on the external cylinder. The robot jumps as the motor causes the spring to undergo compression, followed by a lock-release mechanism [4]. The microcontroller board is attached above the base plate, and performs the necessary controls for the motor and data acquisition for the

sensor. Four batteries on the base plate of the shell provide power, each supplying 3V and a maximum current of 300mA [4].

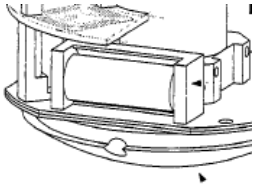

Figure 6 Integrated electrical system with mechanical assembly for hopping robot [4]

The Sandia Hopper, shown in Figure 7, achieves jumping locomotion by firing a piston into the ground, resulting in acceleration of the heavier upper body [10]. Unlike the above mentioned robot, the Sandia Hopper uses the combustion of liquid propane to fire the piston. The robot uses an off-centre control mass to tilt the device in the intended jump direction. Because the energy density of hydrocarbons is higher than that of springs, the robot shows better performance that some of its counterparts, achieving jump heights and distances of 3m.

Figure 7 Piston of Sandia Hopper actuated through combustion of propane

1.2.1 Summary of Macro-Scale Robot Integration

Macro-scale robots require complex mechanics and integration of numerous subsystems built around a single casing or chassis. The electronics used are assembled on PCB and must interface with mechanical actuators to perform a desired task. Integration becomes a tedious manual process involving the use of screws and pins to reinforce both electrical and mechanical elements. The task of assembling and integrating these modules becomes a challenge when the robot is reduced in size and form factor. But ultimately the goal is to achieve similar complex functionality even as the system is scaled down in size.

1.3. Previous Work on Micro-Scale Robots

The ability to adapt to an environment and undertake covert reconnaissance operations requires that the system be scaled down considerably. This has sparked great interest in millimeter and even micron size robots. Like the 1960's film, Fantastic Voyage, the ability to design the modern-day *Proteus*, and miniaturize it for the purpose of traveling through the human body to remove a blood clot, continues to

drive research in the field of microrobotics [12]. Even film writer Harry Kleiner potentially understood the importance of size and functionality in an integrated system. The *Proteus* was miniaturized to one micrometer in length for its exploratory voyage, with the understanding the anything greater than this size scale would cause the nuclear submarine to be detected and attacked by the human immune system. The ability to encapsulate functionality in a micron scale form factor is a challenge that exists for microrobotic systems. PCB and COTS become impossible to implement for Proteus-sized robots. Table 2 summarizes a set of two centimeter scale microrobotic platforms, while Table 3 provides a similar analysis for sub-centimeter microrobots. Both highlight the size, locomotion, actuation, and power requirements for each platform.

Robot	Size	Locomotion	Actuation	Power
RoACH [12]	3cm length	Crawling	Shape Memory Alloy	0.83W @ 10.6V
Jumping Robot [13]	5cm height	Jumping	Springs, Pager Motor	352mW @ 3.7V

Table 2 Summary of design and operation specifications for centimeter scale platforms

Robot	Size	Locomotion	Actuation	Power
Micro-Robot [2]	60μm x 250μm 10μm	Crawling	Scratch Drive	112V (peak), 39V minimum
Walking-Silicon [14]	4mm x 1mm	Crawling	Thermal	1.1W
I-SWARM [15]	23 cubic mm	Crawling	Piezoelectric	300 - 700μW

Table 3 Summary of design and operation specifications for sub-centimeter platforms

1.3.1 Centimeter Scale Micro-Robots

The RoACH Robot

Attempts have been made to reduce the size of the robot platform while still using COTS for system architecture. The RoACH in Figure 8 is fabricated using S2-glass reinforced composites and flexible polymer hinges [13]. This involves a smart composite microstructures (SCM) process where laser micromachined composite

fiber laminates are integrated with polymer films. With laser micromachining, features can be positioned to provide electrical routing to aide in actuation. Sensing, steering, and communication are achieved using a 440mg control electronics board manufactured with 25μm core FR4 fiberglass. The board design is implemented using surface mount components, as well as a connector to power electronics and attach a sensing "daughter card" [13]. Even with the ability to integrate the control electronics on-board the robot, it can be seen from Table 4 that the mass of the on-board power supply accounts for 35% of the entire payload. The electronics needed to control the robot and provide power conditioning make up 28.7% of the payload, of which 44.1% of the mass for the electronics and power conditioning circuit is designated for blank board.

Figure 8 The RoACH robot size comparison to U.S. quarter [13]

28/mg
Power Supply
Structure
Actuators
Wiring

Table 4 Mass comparison of components needed to construct the RoACH [10]

Jumping Robot

The 5cm, 7g jumping robot designed in [14] is capable of jumping over obstacles 27 times its own size. Shown in Figure 9, the jumping robot consists of a gear box, which includes a motor, gearwheels, and cam. To release the energy needed during the acceleration phase of the jump, the robot uses a small pager motor to actuate the cam and rotate the leg lever arm. This process slowly charges and stores energy in two torsional springs connected to the main leg, which can be released on demand. To recharge the mechanism for one jump cycle in 3.5s, 352mW of power is consumed at 3.7V. While this robot requires relatively low power, implementing a similar mechanical design at reduced size scale poses a challenge to both assembly and integration.

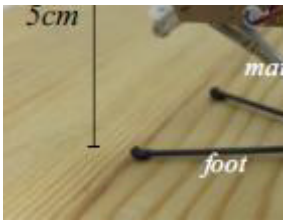

Figure 9 Jumping robot capable of jumping 1.4m in height

1.3.2 Sub-Centimeter Scale Micro Robots

A different approach to the daunting challenge of system integration on a micron scale involves integrating power into the operating environment [2]. The untethered scratch drive actuator designed with a cantilever steering arm in Figure 10, receives "a common power and control signal through capacitive coupling with an underlying electrical grid" [2]. This MEMS microrobot has dimensions of 60µm by 250µm by 10µm. Integration of power, and control schemes into the operating environment allows designers to move beyond the traditional "walking chip" [2]. The major drawback with such an approach is that microrobots must be used in a number of environments that may not be easily controlled, and may change over time. Thus the robotic system must be able to adapt in order to maintain its versatility.

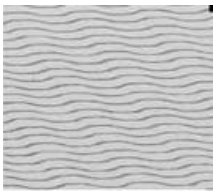

Figure 10 Scratch drive actuator and cantilever steering arm is used to maneuver the robot

I-SWARM Robot

The design of the I-SWARM robot, shown in Figure 11, is based on a fully integrated system platform that provides locomotion, infrared communication, proximity sensing, and on-board power in a cubic millimeter volume. The system is developed using an ASIC, which allows the microrobot to response to external stimuli. This "walking chip" must support a group of amorphous silicon solar cells mounted on a 3.9 by 3.9mm^2 PCB. The limitation to such a multi-functional system lies in the fact that the I-SWARM microrobot must work in a controlled area known as an arena. High intensity lights are projected from above the arena allowing the microrobot to move within the design space.

Figure 11 Conceptual image of I-SWARM robot [15]

Silicon Walking Micro-Robot

Another "walking chip" presented in [7] is designed to carry a maximum external load of 2500mg on its back. The 15mm x 5mm microrobot, while initially lacking on-board sensing and controls, is composed of polyimide actuators that provide walking locomotion. The system is powered by an external power supply that is attached to three 30μm thin gold bond wires measuring 5 to 10 cm in length. Shown in Figure 12, the silicon microrobot is capable of achieving walking speeds of up to 6mm/s at an applied square voltage of 18V at 100Hz. This maximum walking speed is achieved at 1.1W. For such a design, the power budget for additional system components poses a potential challenge to develop an untethered autonomous microrobot.

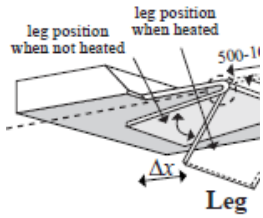

Figure 12 Silicon microrobot with polyimide joint actuators

1.3.3 Summary of Micro-Scale Robot Integration

The integration of electrical and mechanical subsystems on a microrobotic platform requires crude assembly techniques, which add to the complexity and cost of producing platforms in large quantities. Although the RoACH presents a unique integration approach using the SCM process, the overall assembly is complicated by up to 100mm of SMA wire that is controlled by on-board power conditioning electronics. As robotic platforms shrink to the sub-centimeter scale, current designs are unable to meet the power demands and have resorted to off-board power, which severely limits the usefulness and versatility of the robot.

2. Physics of Jumping

Among the various types of locomotion used by robots to explore their environment, jumping enables platforms to travel long distances in a short period of time. In addition to traveling long distances, jumping allows robots to overcome obstacles that are orders of magnitude larger in comparison to their size. This increases the usefulness and versatility of the robot. For many applications, storing and rapidly releasing energy at certain intervals is important and allows robots to extend their lifespan on a mission.

The ability to momentarily defy the odds of gravity to achieve jumping locomotion is not a trivial feat. Nature has provided numerous examples of creatures that jump in order to survive. These creatures use stored energy in their muscles to propel themselves into the air. Attaining specific jump trajectories is dependent on several parameters, including but not limited to, the amount of energy released by the actuator and the mass of the object. In this chapter, an overview of the mechanism behind jumping locomotion is presented. With an understanding of how jumping is achieved, an alternative approach to rapidly releasing stored energy for jumping will be explored in Chapter 3. This involves harnessing the energy released by an exothermic chemical reaction.

2.1 Biological Motivation

Many biological systems rely on the art of jumping, providing insight into the mechanics needed to attain comparable functionality on a microrobotic platform. The 8.5mm long leafhopper Cicadella Viridis, shown in Figure 13, relies on muscular

force that is converted into a force at the feet of the insect to elongate the legs [16]. The cricket, somewhat similar to the grasshopper, uses the large muscle mass of the hind leg through "rapid leveraging movement of the tibia" to jump [17]. In jumping, the front and middle legs are primarily used to alter the position and angle of the body.

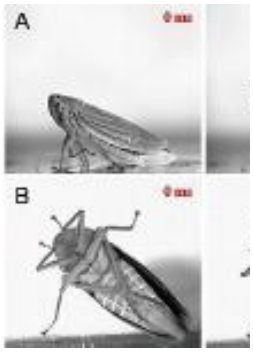

Figure 13 Images of leafhopper Cicadella Viridis hopping showing (A) lateral view and (B) ventral view [16]

While biological systems vary in anatomical structure and body mass, the common thread is the ability to quickly convert stored energy into a constant force. These mechanics are most often modeled by loading and releasing a spring to actuate the microrobot.

2.2 Jump Dynamics

The kinetic energy released by an actuator is critical to achieve jumping locomotion. The ideal jump trajectory is a function of the kinetic energy at take-off, the mass of the object, gravitational force, and take-off angle. In addition to the amount of generated kinetic energy at take-off, the distance and height traveled in

equations (1) and (2) respectively, can be controlled by the take-off angle α of the object.

$$d = 2U_{kinetic} \sin 2\alpha / mg \qquad (1)$$

$$h = U_{kinetic} (\sin \alpha)^2 / mg \qquad (2)$$

To design a jumping platform that can operate in real-world environments, drag forces must be considered. Drag forces oppose the motion of the object through fluid such as air or liquid. From equation (3), the drag force exerted during the jump is a function of the drag coefficient, C_{drag}, the frontal area of the object, *A*, the kinetic energy, $U_{kinetic}$, and the density of air, ρ, through which the object travels. The drag coefficient is a dimensionless number used to quantify the resistance of an object in a fluid. The typical drag coefficient for a short cylindrical body, representative of the hexapod platform, is approximately 1.15 [18].

$$F_{drag} = C_{drag} \cdot A \cdot \rho \cdot U_{kinetic} / m \qquad (3)$$

The height can be reduced by the amount of drag force exerted on the system. At larger take-off velocities the drag force becomes a dominant factor in limiting the maximum attainable height. Table 5 shows the effect of drag on the height as the take-off velocity is varied. The height and distance calculated is based on a 314mg mass, with a take-off angle of 90°, an area of 28mm^2, and a drag coefficient of 1.15. The difference in jump height and distance are compared for an object being

propelled in air and under vacuum. In air, the drag force affects the trajectory. The jump height decreases by 0.2% when drag is introduced at a take-off velocity of 0.80m/s. Increasing the take-off velocity to 2.52m/s, the variation in jump height due to drag is 1.9%. At large size scales, where the area of the object is greater than a few square millimeters, the drag force significantly limits the maximum height and distance traveled. The drag force is proportional to the area of the object being propelled.

KE (J)	Velocity (m/s)	h (vacuum) (cm)	h (air) (cm)	Δh (cm)	d (vacuum) (cm)	d (air) (cm)	Δd (cm)
1.00E-04	0.80	3.2443	3.2378	0.0065	0.5297	0.5296	0.0001
4.00E-04	1.60	12.9716	12.8669	0.1047	2.1189	2.1175	0.0014
8.00E-04	2.26	25.9516	25.5359	0.4157	4.2377	4.2322	0.0055
1.00E-03	2.52	32.4409	31.8093	0.6316	5.2972	5.2885	0.0087

Table 5 The effect of drag and take-off velocity on jump height and distance

Chapter 3: Actuator Design

3.1 Actuators

Actuators enable robotic platforms allowing them to achieve mobility by generating a physical response to a stimulus. This response results in forces and displacements that can be translated into any form of locomotion. To achieve jumping locomotion in particular, several types of actuators are commonly used which include but are not limited to: electro-mechanical, pneumatic, elastic actuators, and propellants. These actuators store and harness energy to produce large impulses, and kinetic energy to generate thrust to propel an object.

Mechanical actuators rely on some mechanical component to convert mechanically stored energy into motion. The electro-mechanical actuators used by the robots in Chapter 1 achieve linear displacements using the rotary motion of a motor. Pneumatic actuators generally consist of pistons and valves that are driven by compressed air. Elastic actuators, such as springs and rubber bands, provide rapid release of stored energy when their structure is compressed and released.

In addition to using mechanical actuators, exothermic chemical reactions resulting in the liberation of heat and gas can be harnessed to achieve thrust. These chemical actuators, to be discussed in further detail, make use of propellants, where the reaction takes place once energy is supplied to a mixture of fuel and oxidizer.

3.2 Mechanical Actuators for Jumping Robots

The Grillo

Mimicking the muscle contraction, joint locking, and elastic tendon stretching of a jumping frog, the "Grillo" robot, shown in Figure 14, uses spring loaded rear legs that are released with a passive click mechanism, providing thrust needed to jump. Failing to achieve continuous jumping, the design was modified using an eccentric cam. The eccentric cam, shown in Figure 14, was used by Leonardo da Vinci to move a hammer. By rotating the cam, the potential energy of the hammer is increased. Once the escape position is reached, the sudden release of energy produces a large peak power [19]. This concept of rapidly releasing energy, therefore converting potential to kinetic energy is important to designing an actuator for jumping. For the "Grillo" robot, the cam "loads a torsional spring that actuates the rear legs."

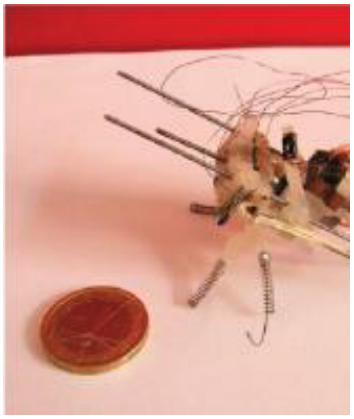

Figure 14 Spring loaded mechanism used to actuate legs with eccentric cam used to store energy

Jumping Robot

The jumping robot shown in Figure 15 is a 5cm, 7g platform that can jump 27 times its own size. This is demonstrated using a cam to charge two torsional springs. The torsional springs are charged using a small 0.66g 4mm DC pager motor, which actuates the cam and rotates a leg lever arm [14]. Energy stored in the springs can be released when a jump is desired. The platform is designed to achieve adjustable take-off angle and jumping force.

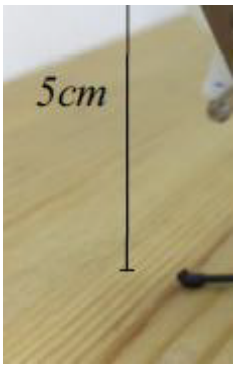

Figure 15 7g jumping robot uses elastic elements in legs to jump up to 1.4m

Cricket Robot

Like the frog, crickets have excellent jumping capability. They can jump up to thirty times their body length, which is about three feet into the air. In [20], the cricket and other insects motivate the design of a jumping microrobot. In contrast to the torsional spring actuator used in the "Grillo" design, the cricket microrobot shown in Figure 16 uses braided pneumatic actuators, known as McKibben artificial

muscles. Shown in Figure 16, this actuator "consists of an expandable bladder inside a tubular mesh made of relatively inelastic fibers [20]." The bladder can be inflated and deflated. When inflated, the actuator contracts because of the inelastic fiber. Power needed to drive the actuators is provided by an on board air compressor. With the use of pneumatic actuators, the leg is able to successfully kick a 1.2 gram paper clip an average of 4.61 inches in the air.

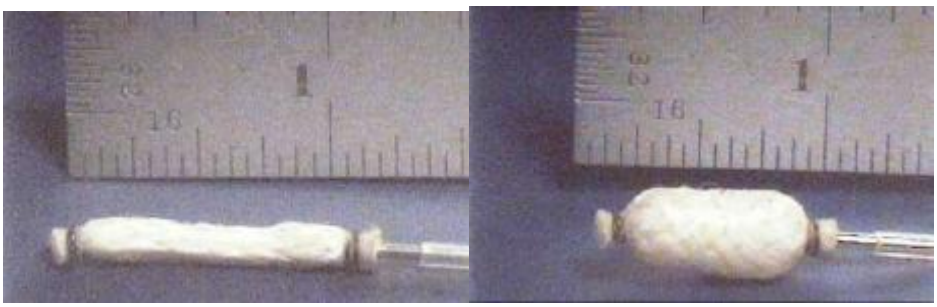

Figure 16 Braided pneumatic actuator used to drive microrobot joints

Elastomer Microrobot

In addition to mechanical actuation with torsional springs and pneumatics, rapid energy release needed to jump has been achieved using micro rubber bands [21]. In [21], a small inchworm motor is used to store energy in a rubber band. The robot shown in Figure 17 is designed with a "micro rubber band attached to the body on one side and a leg connected to a force gauge on the other" [21]. The leg is initially held in place with electrostatic clamps. Releasing 1.2μJ of stored energy in

the leg results in a kick which causes a 0.6mg capacitor to move approximately 1.5cm along a glass slide.

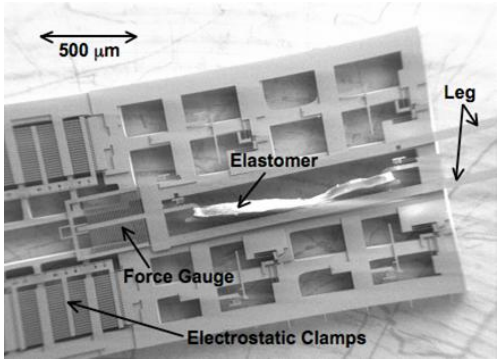

Figure 17 Robot legs held in place by electrostatic clamps

These robots use some form of mechanical actuation to release stored energy to achieve jumping locomotion. Table 6 provides a summary of the type of actuation used by these robots.

Robot	Actuation Principle
Grillo	DC motor loading spring
Jumping Robot	Cam charges two torsional springs
Cricket	Pneumatic actuators/valves with compressed air
Elastomer	Inchworm motor loading micro-rubber band

Table 6 Summary of actuation implemented by several jumping robots

3.3 Chemical Actuators for Jumping Robots

Chemicals known as propellants generate thrust by producing gas. In rockets, bipropellants use a combination of a fuel and oxidizer to generate an enormous amount of thrust to overcome the earth's gravitational field. A fuel is a substance that burns when combined with oxygen, resulting in gas production, while an oxidizer is an agent that releases the necessary oxygen for the reaction. The efficiency of a

propellant is based on the specific impulse, or the number of pounds of thrust obtained when one pound of propellant is consumed in one second.

Two types of propellants are used for jumping actuation, which include liquid propellants and solid propellants. For liquid propellants, the fuel and oxidizer are stored separately, and then mixed and burned to produce thrust. These offer high specific impulse, depending on how the materials are mixed. Common examples include petroleum, cryogens, and hypergols. Solid propellants consist of a mixture of solid compounds (fuel and oxidizer) that are stored together in a casing. Once the compounds are burned, the reaction produces hot gases, which are ejected from a nozzle. The propellant usually burns from the center of the container and propagates outward.

Actuation using propellants for microthrusters is presented throughout literature. In [22] an array of "digital propulsion" microthrusters is fabricated and tested. Each microthruster is composed of a three die stack shown in Figure 18. Microresistors are fabricated on the bottom stack to ignite the propellant. Once ignited, a pressure wave is produced, rupturing the membrane causing an impulse to be generated by the thruster. A 0.5μm silicon nitride diaphragm requiring a burst pressure of 10atm is used as the membrane material. Using lead styphnate as the solid propellant, the microthruster can produce 10^{-4} N·s of impulse at 100W of power. Each chamber produces thrust impulse for approximately 1ms, corresponding to 100mJ of energy. Application of a 30V signal provides the input energy to the resistor to activate the lead styphnate.

Figure 18 Digital propulsion microthruster chip

Chemical actuation of the microthruster shown in Figure 19 is achieved using an ammonium perchlorate (AP) composite propellant [23]. The propellant is formed by mixing fuel and oxidizer with a binder, hydroxyl-terminated polybutadiene (HTPB) and a small quantity of metal powder such as aluminum (AL). The AP in this system acts as the oxidizer, while the binder and the aluminum serve as the fuel. Using HTPB/AP/AL propellant the microthruster can generate 0.76mN to 4.38mN of force, with total impulses ranging from 1.16e-4 N·s to 4.37e-4 N·s. Application of heat to a wire in the ignition slot causes the propellant to ignite, forcing the gas generated by the reaction to expand through the nozzle.

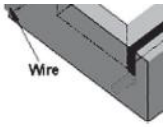

Figure 19 MEMS silicon microthruster designed to ignite solid propellant

3.4 Porous Silicon as an Actuator

While mechanical actuators have the advantage of being reused over time for an indefinite number of jumps, the ability to integrate them on sub-centimeter robotic platforms becomes a unique challenge, as space and power constraints arise. Integrating a pneumatic piston or high voltage actuator is not trivial at small scales. As a result, low input energy and high output force gives propellants a unique advantage over mechanical actuators, especially in applications where a limited number of jumps is needed.

Most propellants require the mixture of a fuel and oxidizer, which result in an exothermic reaction once energy is supplied to the system. Many of the lead-based propellants are mixed in a slurry form, making it difficult and messy to package. In addition to propellants, nanothermites produce exothermic reactions when ignited. Nanothermites are composed of a mixture of an oxidizer and a reducing agent that are mixed at the nanoscale. In contrast to traditional thermites, the reduction of the

oxidizer and reducing agent to nano-scale particle sizes enhances the reactivity of material. Ignition can be achieved using heat, impact, or electrostatic discharge. The most significant challenge associated with nanothermites is the ability to integrate a nano-scale powder on-chip. As a result, nanoporous energetic silicon is chosen as the chemical actuator for the jumping hexapod. It can be ignited in a similar fashion as nanothermites, but has the added benefit of being integrated directly on-chip using bulk micromachining techniques. The fuel used by this chemical actuator is silicon. Once a liquid oxidizer is applied to the porous material and dried, the energy output capability can surpass some traditional energetics. Table 7 presents a comparison of nanoporous energetic silicon with commonly used nanothermites.

Material	Burn Rate (m/s)	Input Energy (μJ)
CuO/Al [24]	1500	231
Bi2O3/A [24]	350	309
MoO3/Al [24]	140	427
Porous Si [25]	1590	180

Table 7 Comparison of nanoporous energetic silicon with nanothermites

An added benefit to nanoporous energetic silicon lies in the relatively low input energy and the increased burn rate. The reaction burn rate is proportional to the pressure and initial temperature of the reaction as shown by Saint Robert's Law in equation (4), where r_b is the burn rate, P_c is the chamber pressure, a is an empirical constant that depends on the initial temperature, and n is the pressure exponent [26]

$$r_b = aP_c^n \qquad (4)$$

3.4.1 Overview

Porous silicon has emerged as a new energetic material; with measured energy output more than double that of TNT [27]. Similar to modern bipropellants, porous silicon can be used as an actuator when mixed with an oxidizer. Because it is easily fabricated on p-type, 1-20 ohm-cm, boron doped silicon wafers, it can be integrated alongside MEMS devices using bulk micromachining techniques. Further details on fabrication and integration with Microelectromechanical systems (MEMS) can be found in [27]. In addition to its ease of integration, nanoporous energetic silicon offers a "green" alternative to propellants which contain traces of lead.

While the energetic output of the reaction can be tuned by controlling the porosity of the porous silicon [25], the oxidizer (sodium perchlorate) is hydrophilic, and tends to absorb moisture from the atmosphere. This reduces the energetic output of the nanoporous energetic silicon. Based on sensitivity tests, the material is relatively sensitive to electrostatic discharge and impact. These challenges require new techniques in packaging to increase lifetime and reduce sympathetic ignition. Despite these downsides, the potential for integration with MEMS makes this actuator attractive for the microrobot in this thesis.

3.4.2 Actuation using Energetic Nanoporous Si

Actuation used to generate the jumping locomotion of the hexapod microrobot is based on an exothermic chemical reaction that takes place between nanoporous silicon and an oxidizer, sodium perchlorate. The nanoporous silicon is inert prior to applying the oxidizer. Once infused with the oxidizer, the reaction can be triggered

using heat, friction, or focused light [27]. Figure 20, shows ignition of the nanoporous energetic silicon via a spark. The reaction that takes places is described in the following chemical equation [27]:

$$nSiH_2 + (1-n)Si + \frac{(2+n)}{4} NaClO_4 \rightarrow SiO_2 + NaCl + nH_2O + heat$$

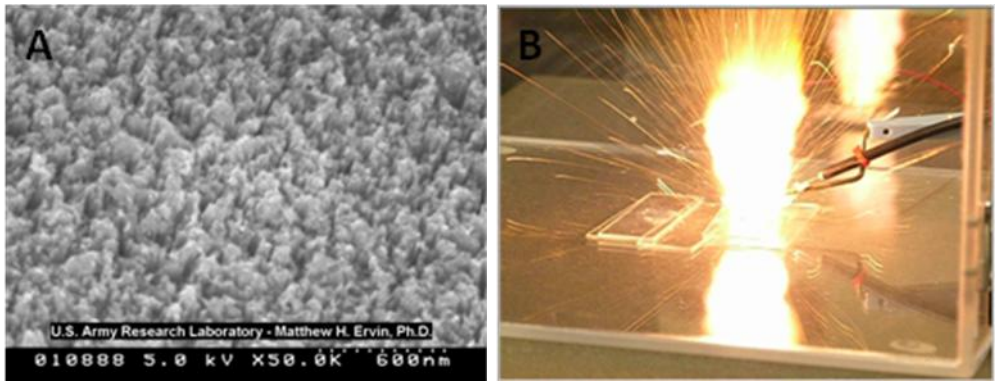

Figure 20 A. Top down view of nanoporous silicon before application of oxidizer. B. Ignition of 1cm diameter nanoporous energetic silicon sample with spark.

Several energetic regions can be patterned on a single chip to provide multiple jump capability. Figure 21, shows four-2mm samples that have been etched. The adjacent samples are isolated from each other by a layer of LPCVD low-stress nitride, which protects the underlying silicon from being etched. Each 2mm region of nanoporous silicon has a lithographically patterned initiator wire.

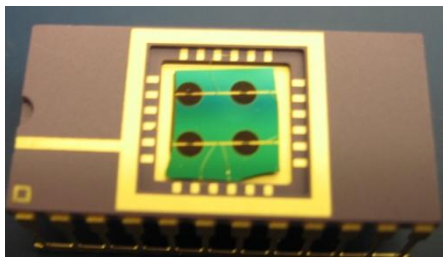

Figure 21 Four individually addressable 2mm nanoporous energetic Si devices

In [28] an aluminum foil flyer experiment was conducted to determine the amount of thrust generated from the reaction. A 40mg flyer, shown in Figure 22, was placed on top of a 5mm diameter nanoporous silicon sample, but was not attached. The depth of the porous silicon layer is approximately 40µm. Using a high-speed video camera recording at 1000 frames per sec, and neglecting air resistance, it is shown that the flyer travels a maximum height of 1.27m, with a measured initial translational velocity of 5m/s. A translation kinetic energy of 500mJ is exerted by the 40mg flyer. Based on observation that the light from the reaction is visible for 3 frames, the time of the impulse is estimated as 3ms. Dividing the change in momentum by the time of the impulse, it is shown that the equivalent force exerted on the flyer is 67mN. From the area of the porous silicon device, the equivalent pressure produced over the area is 3.4kPa [28]

Figure 22 Thrust demonstrated to propel an aluminum foil flyer

To generate sufficient thrust to propel a flyer, the reaction of the nanoporous silicon results in the generation of gas as well as particulates [27]. Gas production is quantified using a sealed calorimeter bomb. From [27] it is shown that for 4 nanoporous silicon samples etched at 18.4mA/cm^2 in 1:1 HF/Ethanol solution, 5.6e-4

moles of gas are produced by the reaction. 70% of the measured gas generated is due to the hydrogen being oxidized to vapor phase H_2O. While the gas generation per gram of active mass for the best modern day propellants is on the order of 0.045 mol/g [29], the measured data in [27] indicates that with a gas generation of 0.0189mol/g of active mass, the nanoporous silicon has the potential to out-perform conventional propellants.

The ability to out-perform some conventional propellants while being able to easily and inexpensively fabricate the energetic on chip with MEMS provides a novel actuator. Rather than developing a thruster package, and adding the propellant after post-production, the nanoporous Si (fuel) and oxidizer can be integrated directly into the system, and mixed once the material is ready to be energized. Because integration is a key benefit of using a silicon-based energetic, adding "smarts" in the form of sensing and control circuit provides a fully integrated package that can sense and respond to a stimuli to generate on-board thrust. This holds great potential for designing an autonomous jumping microrobot.

3.4.3 Actuation Requirements

Actuation requirements to achieve jumping locomotion for a 314mg robot platform at a take-off velocity of 1.25m/s are outlined in Table 8. The take-off velocity is chosen based on an approximation of the kinetic energy resulting from a similar size object being propelled by the nanoporous energetic silicon. The velocity can vary depending on the energy output. Actuation of the nano-energetic is demonstrated at a maximum power of 2.35W for duration of 200μs, where the

maximum power is the maximum voltage and current supplied to the initiator to ignite the nanoporous silicon. Even at 2.35W, the input energy supplied to the initiator is 125µJ because the power is not constant over 200µs. The mass of the energetic material in the 2mm diameter sample is 0.21mg, where the thickness of the energetic nanoporous silicon layer is 75-82µm.

Requirements	
Kinetic Energy of Hexapod	246µJ
Mass of Actuator (including bulk Si)	38.6mg
Total mass of Hexapod	314mg
Take-off Angle	90°
Input Voltage	<5V
Input Power	2.35W for 200µs
Input Energy	125µJ

Table 8 System requirements for nanoporous energetic silicon

Applying the system requirements in Table 8, an approximation of the jump height is modeled in Figure 23 using MATLAB. For the model, it is assumed that the cross-sectional area of the hexapod is approximately 28mm^2 and the take-off angle is 90°. Based on a small cylindrical geometry, a drag coefficient of 1 is assumed for the model. Because drag does not dominate at this size scale, there is little difference between the trajectory before and after drag is applied to the model.

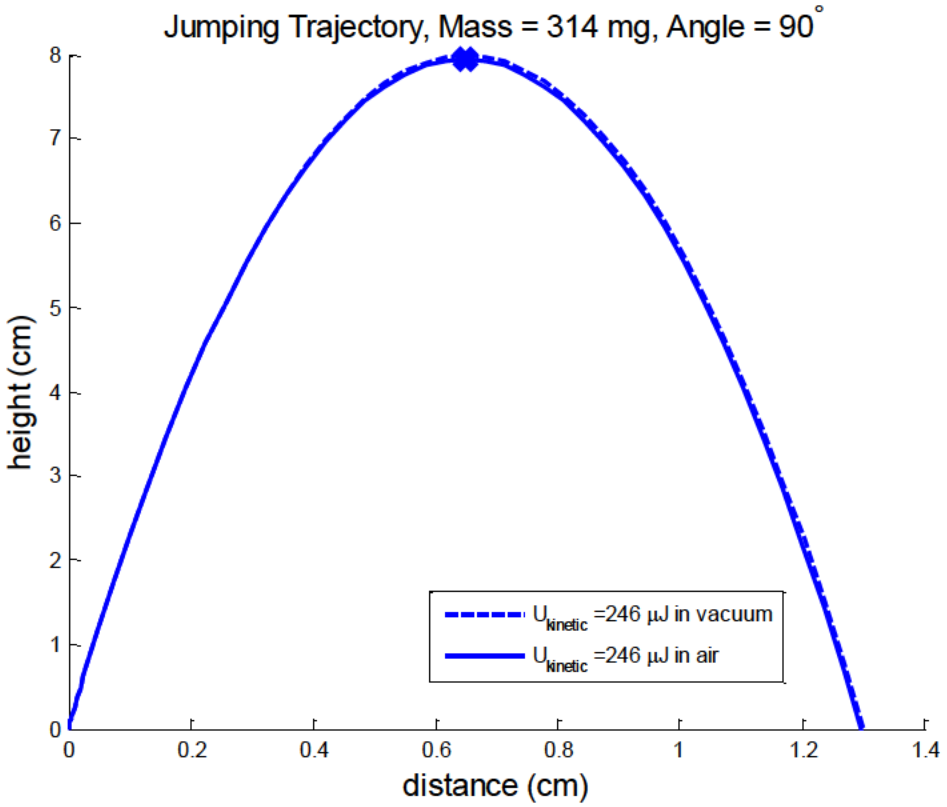

Figure 23 Jump trajectory for a 314mg hexapod modeled using MATLAB

Based on the requirements needed to ignite the nanoporous energetic silicon, in conjunction with the ability to generate sufficient kinetic energy, the hexapod should be able to achieve a jump height of approximately 8cm. This jump height is more than 16 times the height of the hexapod platform. The use of nanoporous energetic silicon appears to be feasible where the robotic platform must traverse centimeter scale obstacles. The jump height can be changed if the kinetic energy generated by the reaction can be modified.

Chapter 4: Sensor and Control

A relatively simple circuit is integrated with the hexapod platform to achieve jumping locomotion of 8cm in vertical height. To meet the demands of designing an autonomous platform on a sub-centimeter scale, the circuit must provide on-board power for optical sensing, and ignition of an energetic material while confined to a $28mm^2$ chassis. Although sensing capability has been demonstrated, this work is the first of its kind to show integration of electronics and nanoporous energetic silicon on a sub-centimeter polymer robot, where minimum feature sizes are below 450µm.

In this chapter, a simplified circuit without any sensing capability is first demonstrated. The circuit is designed to charge up a capacitor connected to an external power supply, then discharge the capacitor through a thermal initiator on the energetic porous silicon once disconnected from the power supply. Based on experimental data gathered from these experiments, a large scale breadboard prototyped circuit is designed, which demonstrates sensing and actuation. Because of the limited chassis area (4mm by 7mm) and payload, as dictated by the size of the microrobotic platform, this circuit is then reduced in size to drive a sensor at 5VDC, while providing power to ignite the nanoporous energetic silicon.

4.1 Circuit Design

The circuit, which provides the microrobot with a unique level of autonomy, consists of two modules, a sensor and actuator module, operated with on-board power. Rather than using on-board batteries which are difficult to obtain at these size scales, power is supplied by capacitors that are charged prior to operating the circuit.

The circuit allows the hexapod to detect a change in light intensity, and delivers a 5VDC signal to a thermal initiator triggering the ignition of a chemical actuator (nanoporous energetic silicon). Ignition of the energetic generates a rapid pressure wave, causing the hexapod to be propelled upward in a jumping motion.

4.2 Capacitor Switch Test

The first step is to confirm that the energetic material can be initiated using only a charged capacitor as a power supply. Based on characterization of the thermal initiator, a circuit is designed that charges up a capacitor and physically isolates it from an external power supply before supplying the charge to a load resistor. The load resistor, R_{load}, in Figure 24 is used to model the electrical resistance of the thermal initiator. The circuit is constructed using a 10µF, 16V capacitor in series with a toggle switch that is in series with the load resistor.

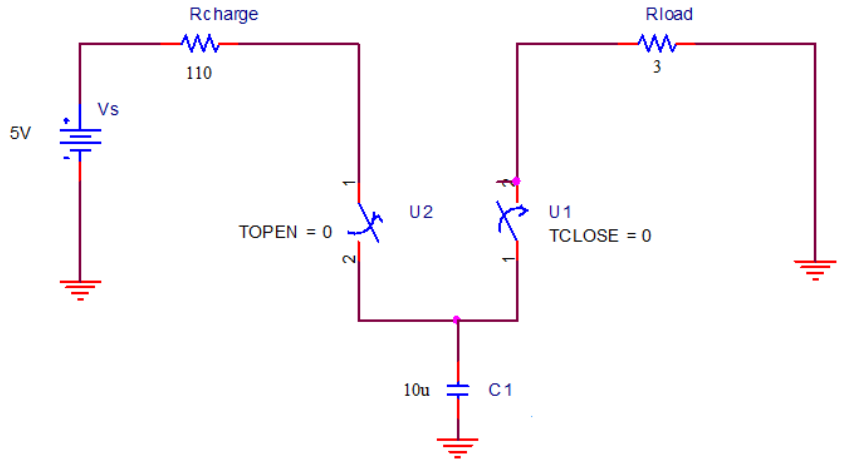

Figure 24 Switching circuit used to charge and discharge a capacitor to ignite actuator

Figure 25 shows the voltage versus time as a capacitor discharges through the resistor in approximately 200µs. The capacitor is initially charged to 3V for this experiment.

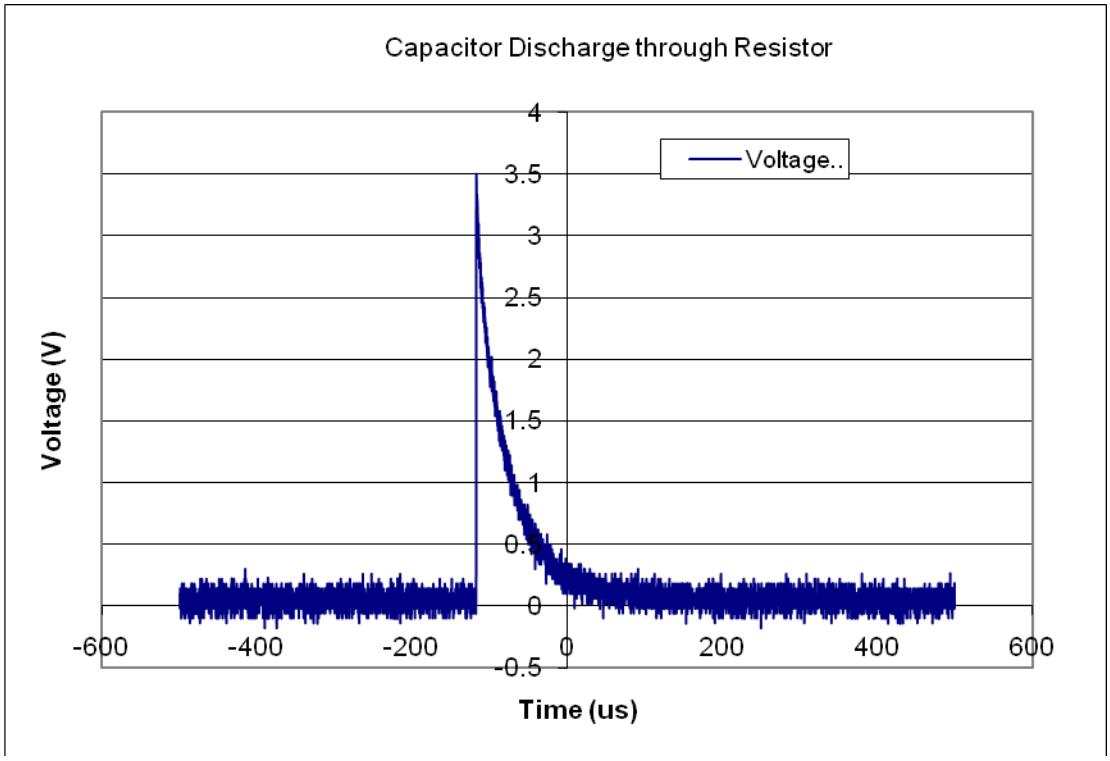

Figure 25 Discharge of 10µF capacitor through 3Ω resistor using the simplified switching circuit

Ample time must be allowed for the initiator to heat up, at which point the porous silicon ignites and the current across the initiator drops to zero due to the resistor rupturing. Figure 26 shows experimental data, comparing the voltage and current across the thermal initiator with respect to time. For an initiator measuring 15µm in width by 75µm in length, the initiator ignites the energetic at time t ~ 120µs. In Figure 26 the current and voltage are initially zero before application of a 5VDC signal. The voltage and current across the initiator increase, resulting in heating of the sample. Heating triggers the exothermic reaction, causing the initiator to rupture, at which point the current drops to zero. The voltage spike is an artifact of the power supply. The load resistor, in Figure 24, is then replaced with an active 2mm diameter

energetic device. Each 2mm energetic device is wirebonded to pins on an electronic dual in-line package (DIP). The DIP is placed in series with the charged capacitor before the switch is closed to connect the energetic device to the capacitor. The 2mm energetic device is successfully ignited using the 10µF capacitor as a power supply.

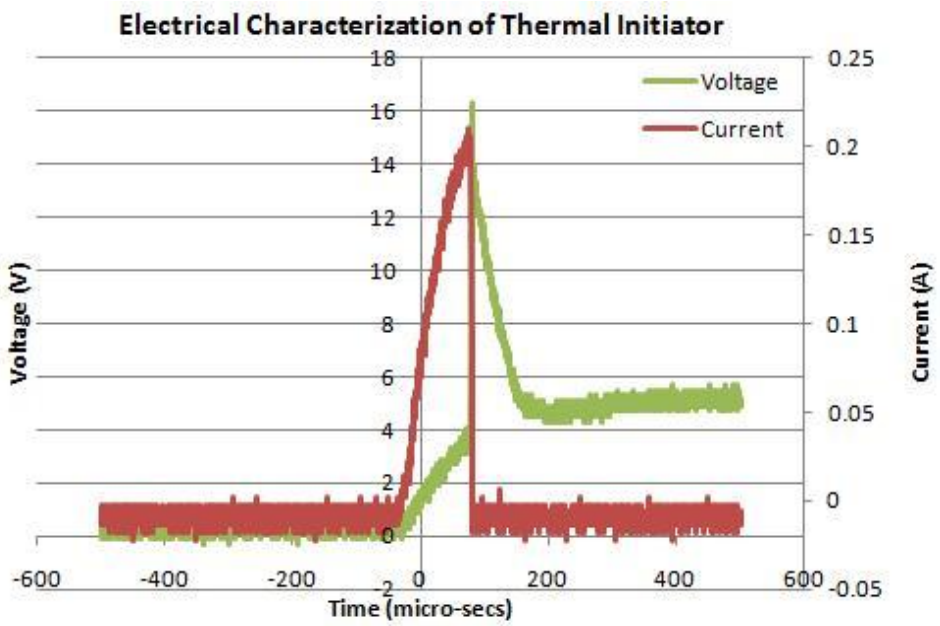

Figure 26 Electrical response of thermal initiator used to actuate energetic

From this experiment, the voltage requirements needed to ignite the nanoporous energetic silicon without having to physically connect the initiator via wires to an external power supply are confirmed. Using a relatively small, 10µF capacitor, between 3.5VDC and 5VDC can be supplied to the initiator to trigger the energetic reaction.

4.3 Large Scale Circuit Prototype

Based on the previous demonstration, an initial breadboard prototype is developed to achieve optical sensing and ignition of the actuator. While not constrained by the size limitations of the microrobotic platform, the goal of designing the large scale prototype is to determine the necessary functional components needed to adequately sense a change in light intensity and achieve a jump.

For this circuit, the operational requirements are fast switching speed and minimal leakage current. This is achieved by using a LM393 comparator to generate a TTL signal to turn on the gate of an IRF540N n-channel power MOSFET, whose on-resistance is 0.040Ω at V_{GS} equal to 10V. The IRF540N was arbitrarily chosen due to its availability. The leakage current is approximately 100nA for V_{GS} equal to 20V. While the transistor is overrated for the necessary application, it has a maximum turn-on time of 100ns when operated at V_{GS} equal to 10V. At 5VDC, the operating voltage level for the sensing circuit, the maximum drain current is approximately 40A. This presents a serious concern for power dissipation and heating the circuit.

The comparator and MOSFET are controlled by an NPN silicon phototransistor. The on-state maximum collector current is equal to 50mA, while the dark current is equal to 100nA with V_{CE} equal to 10V. At 5VDC emitter-collector voltage, the continuous collector current is 50mA. Working together these components provide an elegant circuit to sense, but require significant power draw, as the phototransistor itself draws up to 250mW at 5V.

4.3.1 Large Scale Circuit Operation

The circuit consists of three major components: OP599A phototransistor, an LM393 comparator, and IRF540N transistor. The OP599A has a peak spectral sensitivity at 850nm. When exposed to light at its peak sensitivity, it supplies approximately 50mA of continuous collector current. Illumination of the circuit shown in Figure 27 using an 850nm light source causes the non-inverting input voltage of the LM393 comparator to remain low and the IRF540N switching transistor remains in the off state. Once the light source has been blocked from the path of the phototransistor, the internal resistance of the phototransistor increases, resulting in a high voltage at the non-inverting input of the LM393 comparator. The biasing voltage can be supplied to the inverting terminal in order to get the reverse effect, where application of the light source forces the output of the comparator high. The gate of the n-channel enhancement mode transistor then turns on, providing a path to ground for an already charged capacitor to discharge through the integrated initiator. This capacitor discharge ignites the energetic material. The schematic, shown in Figure 27, implements hysteresis to prevent small output voltage fluctuations due to noise that is typically present at the input. Figure 28 shows the discharge current through the initiator wire, which is represented by resistor, R7, once light has been detected.

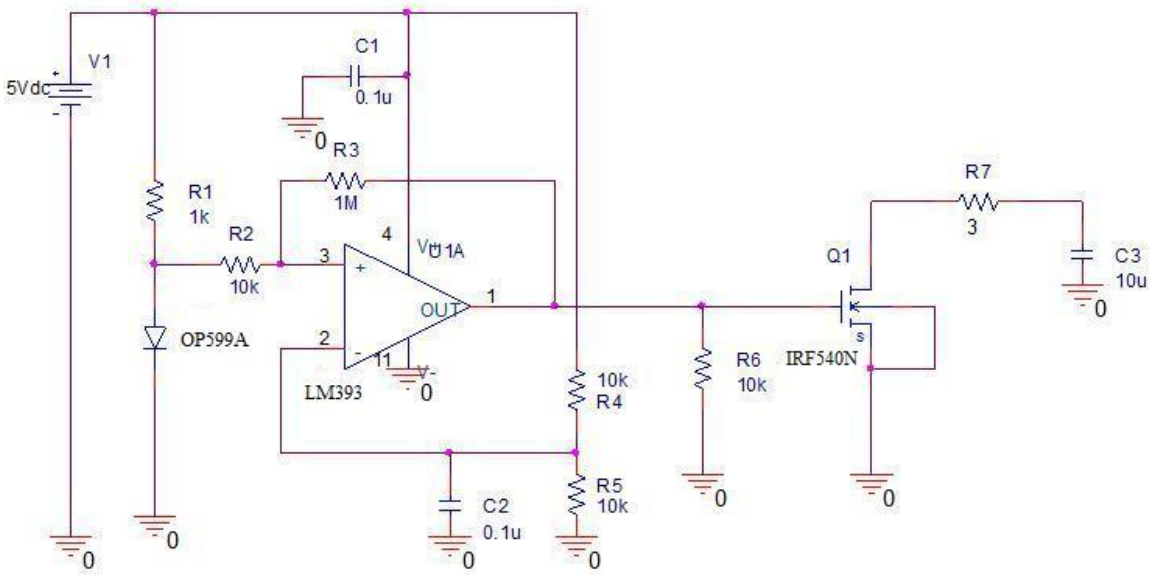

Figure 27 Schematic of circuit with light sensor used to detect and thermally ignite porous silicon.

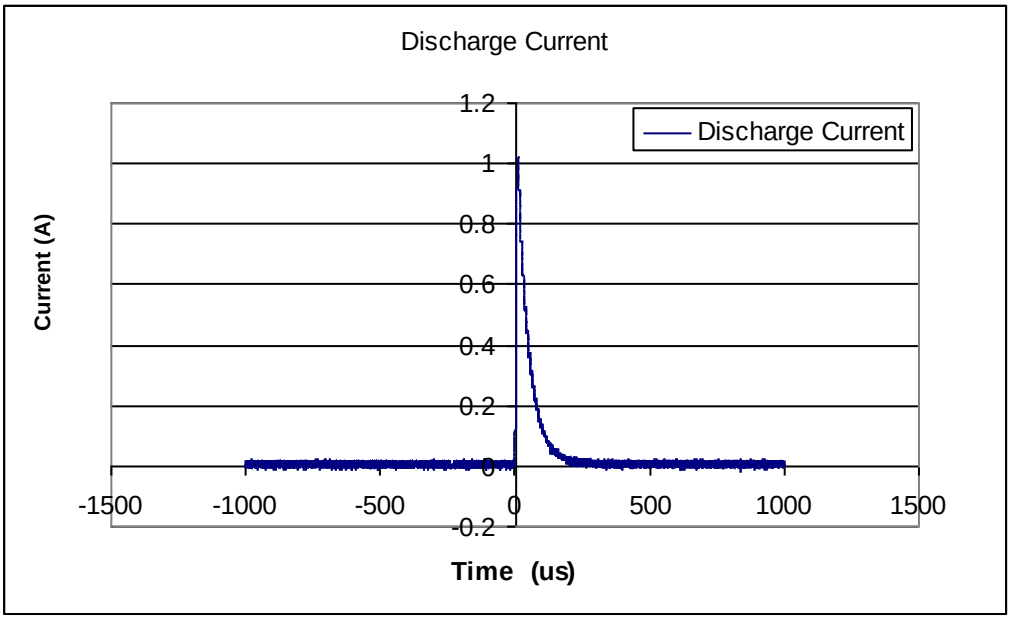

Figure 28 Discharge current through resistor when capacitor charged to 5V

4.4 Miniaturized Circuit

While this large scale circuit satisfies the initiator requirements, the space available to integrate electronic controls for sensing and actuation is limited to a

$28mm^2$ area. As a result, the large scale prototype circuit is reduced to accommodate a phototransistor for sensing and a transistor for switching. Implementation of a scaled down version of the circuit is demonstrated using a SFH3710 silicon NPN phototransistor. The operating requirements still require fast switching and minimal leakage current, while minimizing the power dissipated. For V_{CE} of 5VDC, the collector current in the on-state is equal to 20mA, which corresponds to 100mW of power. The dark current is on the order of 3nA. To maintain fast switching, a 2N7002 n-channel enhancement mode field effect transistor is used. The maximum drain current is greater than 115mA, which provides enough current to trigger the energetic, with a reduction in the maximum power dissipation to 200mW.

4.4.1 Miniaturized Circuit Operation

Because the circuit, shown in Figure 27 is too large to implement on a millimeter scale hexapod platform, the complexity of the circuit is reduced by removing the hysteresis and using an n-channel enhancement mode field effect transistor as a switch to discharge the capacitor through the initiator wire. The output of the comparator in the original large scale circuit design shown in Figure 27 provides the necessary TTL signal to supply sufficient turn-on voltage to the gate of the transistor, allowing it to turn on fast enough to source current through the initiator wire. The modified circuit, shown in Figure 29, is composed of five COTS components, which include a 100μF and 10μF capacitor to supply power, a 10kΩ resistor, a SFH3710 phototransistor, and an n-channel enhancement mode 2N7002 MOSFET. The 100μF capacitor is charged to 5VDC, providing the necessary

operating voltage to power the phototransistor. Similar to the large scale circuit, the response of the phototransistor causes the gate of the FET to turn on when light has been detected. The spectral sensitivity of the NPN phototransistor is 350nm to 950nm, with a maximum sensitivity wavelength of 570nm. At a gate-source voltage of 5VDC, the drain current of the MOSFET is on the order of 1A. The MOSFET is chosen to provide sufficient drain current at a moderately low gate voltage. A rise in the gate voltage causes the 10μF capacitor, charged to 5VDC, to discharge through the 3Ω resistor. The 3Ω resistor is included in the circuit design to simulate the initiator wire.

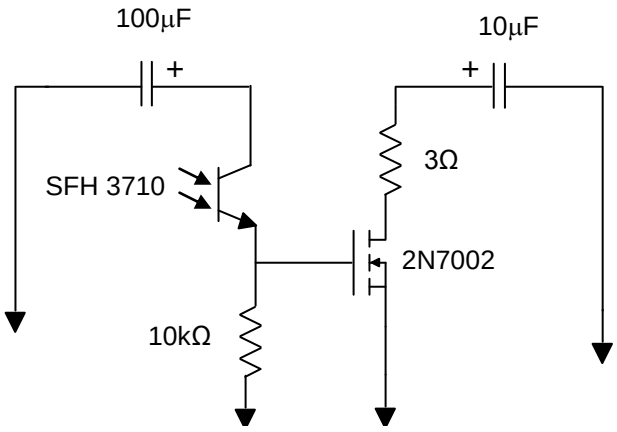

Figure 29 Miniature circuit with sensing and actuation capability

4.5 Cadence Model

The simplified circuit, shown in Figure 30, is simulated in Cadence to analyze the drain current when the phototransistor is in its on-state and off-state. The phototransistor is modeled as a resistor, whose value is changed depending on the lighting condition. Using a multimeter, the internal resistance of the phototransistor is measured under two different lighting conditions. For off-state conditions, the

fluorescent lights are turned off, except for a small desk lamp in the opposite corner of the room, resulting in an internal resistance of 30MΩ. Eliminating the desk lamp increases the resistance above the limit of the multimeter. The on-state resistance is measured after illuminating the optical sensor with a 3-LED circular array. The LED array, used for videostrobe and flood exposure is positioned approximately 10cm above the optical sensor. The on-state resistance is less than 45Ω at a luminous output of 750 total lumens. A 2N2222 NPN BJT is used to demonstrate switching in the circuit. Simulations are run to determine the collector current through the initiator as a function of the lighting conditions.

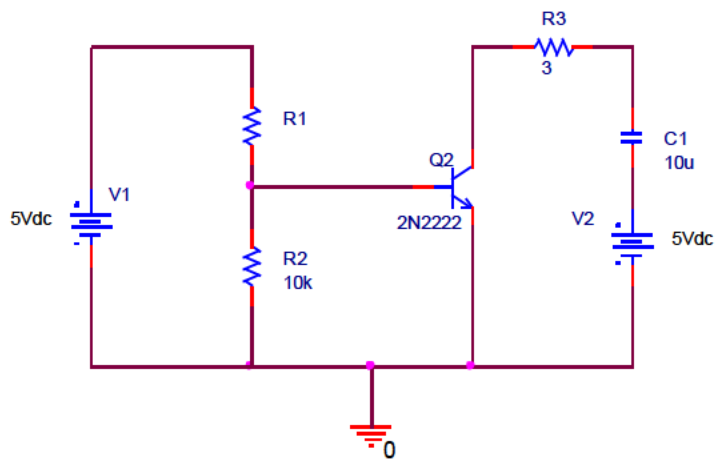

Figure 30 Circuit modeled in Cadence

In Figure 31, the phototransistor is illuminated and the on-state resistance drops below 45Ω. A collector current of 900mA is supplied to the initiator. At time t=0, there is a transient response as the current across the 3Ω load resistor increases prior to reaching steady state.

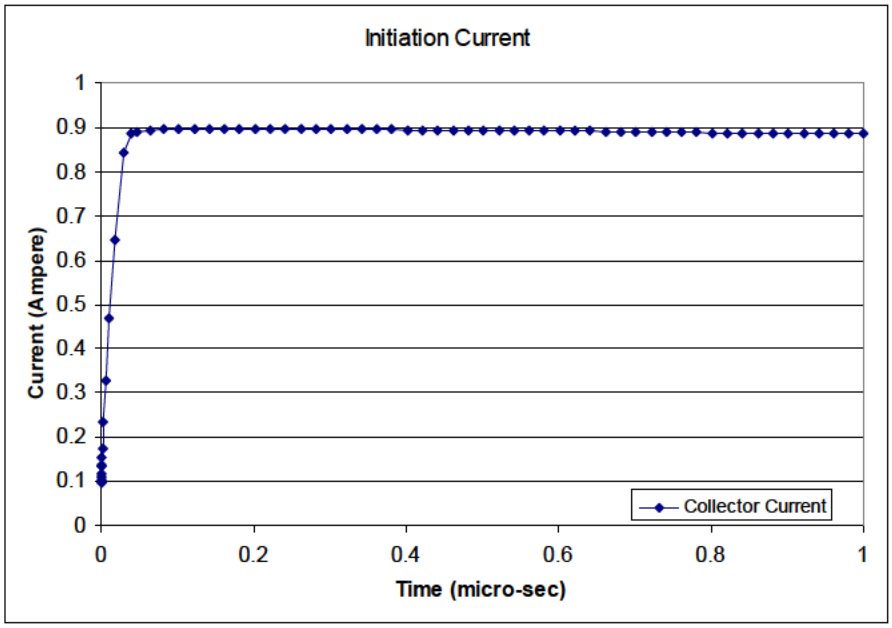

Figure 31 Current as light is shown onto the circuit

For off-state conditions where no light is supplied, Figure 32 shows a zero current across the initiator after reaching steady state at time t~0.08μs. At time t =0, there is an initial 150mA current spike, which is most likely a transient effect. The discharge voltage is an exponential function shown in equation (5), where V_o is the initial voltage stored at time t=0, and RC is the time constant associated with the circuit. Figure 32 is representative of this exponential decay behavior.

$$V_c=V_o e^{-t/RC} \qquad (5)$$

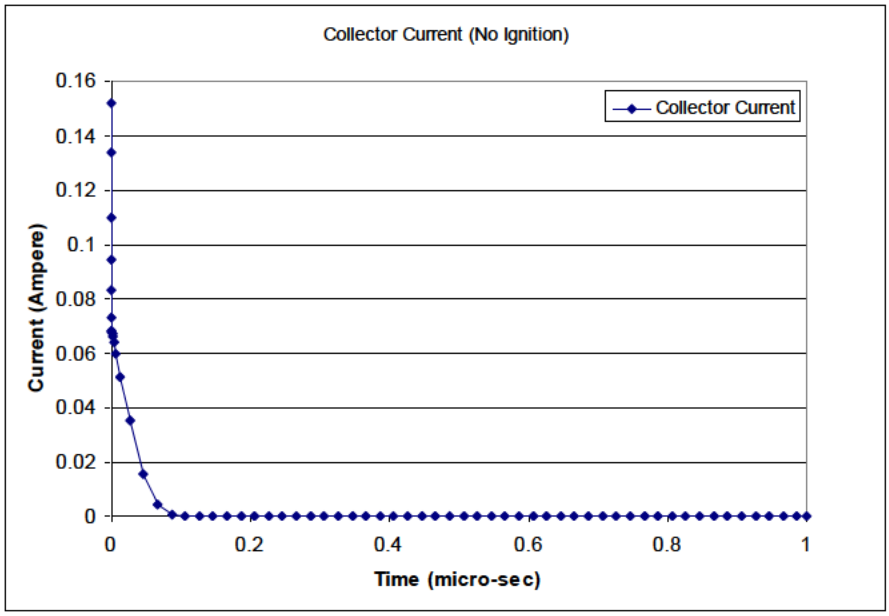

Figure 32 Current level when no light is detected by the circuit

In addition to supplying current to the initiator under lighted conditions, the self discharge of the 100μF power supply capacitor over time is analyzed. The 100μF capacitor supplies power to the phototransistor. Unless the circuit is operated in a completely dark environment, the 100μF capacitor will lose charge because of leakage through the phototransistor. If the voltage drops below a critical level, less than 4V, the MOSFET will remain off, failing to discharge the 10μF capacitor. At this voltage, the gate of the 2N7002, used in the actual circuit, is unable to drive drain current through the thermal initiator. Figure 33 shows the discharge rate for the 100μF capacitor under dark conditions where the resistance of the phototransistor is 25MΩ. After approximately 8 minutes the voltage on the capacitor drops below 4V, at which point the sample will not ignite. The gate voltage is no longer sufficient to turn on the transistor.

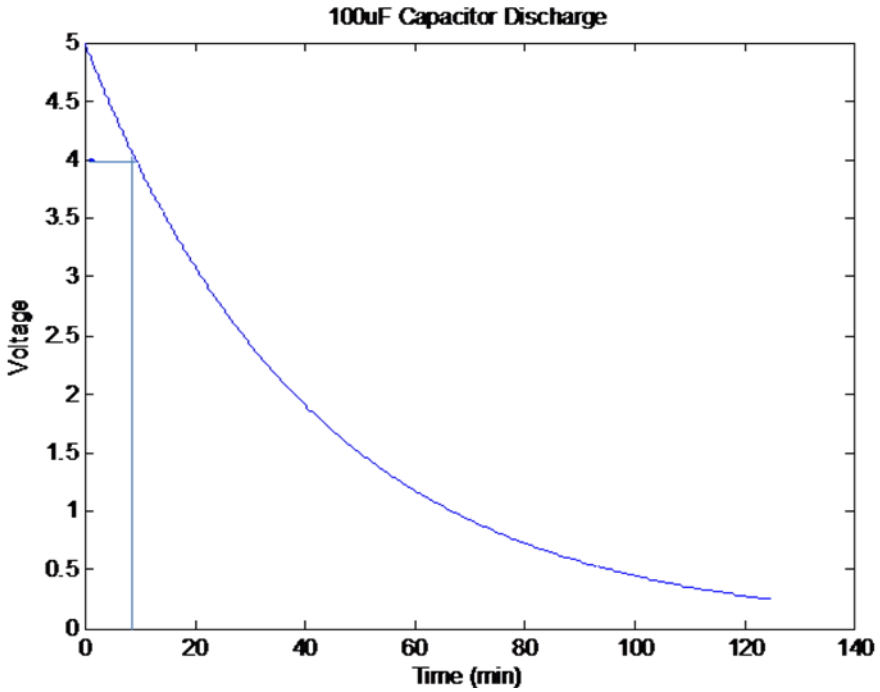

Figure 33 100µF capacitor discharge time in dark condition

Successful implementation and testing of the control circuit on a millimeter scale footprint has been demonstrated prior to integrating the system onto the robotic platform, which will be discussed in Chapter 5. Transitioning from a large breadboard level design to a millimeter scale platform provides a number of advantages to realizing an autonomous microrobot. The miniaturized circuit allows for significant reduction in weight, while providing functionality similar to the breadboard level design. It meets the unique requirements for supplying on board power, using on-board capacitors to power an integrated sensor and actuator, and increases the usefulness and operational space that can be explored by a microrobot.

Chapter 5: Integration

The design of an autonomous microrobot, with the ability to sense and respond to changes in its environment, is based on fully integrated sensors, actuators, and controls. As mentioned earlier, integrating these components into single system architecture is trivial on a macro scale, where relatively large COTS components and batteries can be assembled and mounted. At the sub-centimeter scale, a unique challenge exists to provide comparable functionality in a very small area. In addition to the size constraints of the circuit components, payload and power requirements must be met to sustain operation. To develop an intelligent robot at this size scale, two types of integration can be implemented: hybrid and monolithic. Hybrid integration usually involves separately fabricating the electrical circuit and the MEMS device, and integrating the two using some packaging technique such as flip chip bonding. Monolithic integration can be classified as a mixed MEMS-IC process, MEMS-first process (pre-IC or pre-CMOS), or an IC-first process (post-IC or post-CMOS) [28]. The design of the Analog Devices' accelerometer provides an example of a mixed MEMS-IC process [30]. Sandia National Laboratories has developed a unique MEMS-first process, where the MEMS device is fabricated "in a trench on the surface of a wafer" [30]. Once fabricated, the wafer is planarized and the trench is sealed, allowing for the wafer to be processed at a CMOS foundry. Because most CMOS foundries do not accept pre-processed wafers, the post-CMOS approach to monolithic integration is most commonly used [30].

In this chapter a hybrid integration approach is described, where the control circuit is fabricated and assembled on a 500μm thick silicon-silicon nitride substrate

using the smallest available COTS parts. Alternatively, a modified hybrid approach is presented where electrical interconnects are fabricated directly onto the polymer chassis of the robot, reducing the overall mass, while still providing on-board power. The polymer used for the robot chassis is Loctite®3525. Assembly is achieved using a low temperature solder dipping process to overcome some of the inherent limitations of using a non-rigid substrate to integrate functionality for an autonomous microrobot.

5.1. Integration on Silicon

Printed circuit boards (PCB) are widely used in semiconductor manufacturing to populate silicon integrated circuit (IC) components that eventually find their way into today's light emitting diode (LED) TV's and personal computers. While these boards are an exceptional choice for large scale systems, the size and weight due to layers of copper traces and epoxy resin add to the payload for a sub-centimeter package that must navigate while carrying its own smarts and power. To overcome this challenge, silicon is chosen along with a light weight polymer as the structural material to integrate a circuit on a sub-centimeter platform.

5.1.1 Hybrid Integration on Silicon Substrate

To accomplish this, electrical traces are first patterned on a rigid 4 inch silicon wafer with a thin film dielectric silicon nitride layer to provide electrical isolation from the underlying silicon substrate. The 8000Å low-stress LPCVD silicon nitride film is deposited by Rogue Valley Inc. AZ5214 photoresist is spun on the wafer, and

the electrical traces are patterned using a reverse image photolithography process. To reverse the polarity of the resist, the wafer is first exposed using a Cr mask to transfer the pattern to the wafer, followed by a post-exposure bake and a flood exposure. AZ300 developer is used to develop the features on the wafer. The metal traces are then deposited using e-beam evaporation of chromium (Cr) and gold (Au), where the chromium serves as an adhesion layer. Once the metal has coated the entire wafer, the wafer is then submerged in an acetone lift-off bath at room temperature to remove excess Au, leaving behind the metal traces. Figure 34 shows patterned electrical traces on a Si wafer.

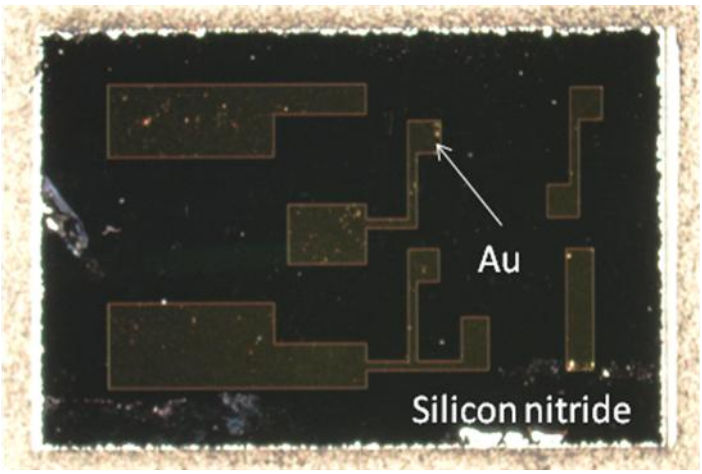

Figure 34 Au electrical traces lithographically patterned on silicon nitride

5.1.2 Circuit Assembly of Silicon Substrate

Once electrical traces have been fabricated on top of the silicon nitride, the miniaturized circuit identified in Chapter 4 is assembled using the smallest available surface mount components. At this size scale it becomes difficult to use a solder iron to make electrical connection. The heat generated by the solder tip causes the 200nm Au traces to delaminate. The circuit is assembled using a low temperature molten-alloy dipping process similar to that presented in [31]. The silicon nitride chip, with

lithographically defined Au binding sites, is dipped into an 80ºC bath of acidic ethylene glycol and a submerged, liquefied Indium-Bismuth-Tin-Lead-Cadmium solder alloy with a 47ºC melting point. The use of ethylene glycol is important to prevent contamination of surfaces that result from metal oxides [31]. Hydrochloric acid is added to the ethylene glycol to reduce the pH and clean surface oxides that form on the molten alloy [32]. Problems related to alloy corrosion and intermetallic compound growth have been avoided by working with an alloy that has a 47ºC melting point [31]. When the wafer, with its Au binding sites, is dipped and retracted through the In-Bi-Sn-Pb-Cd and ethylene glycol interface, the alloy selectively coats the Au binding sites. The low contact angle between the ethylene glycol and the Si or dielectric layer prevents the alloy from wetting the rest of the substrate [31]. Figure 35 shows a similar process developed in [32] to coat metal alloy on titanium tungsten/gold (TiW/Au) interconnects that have been patterned on a plastic substrate.

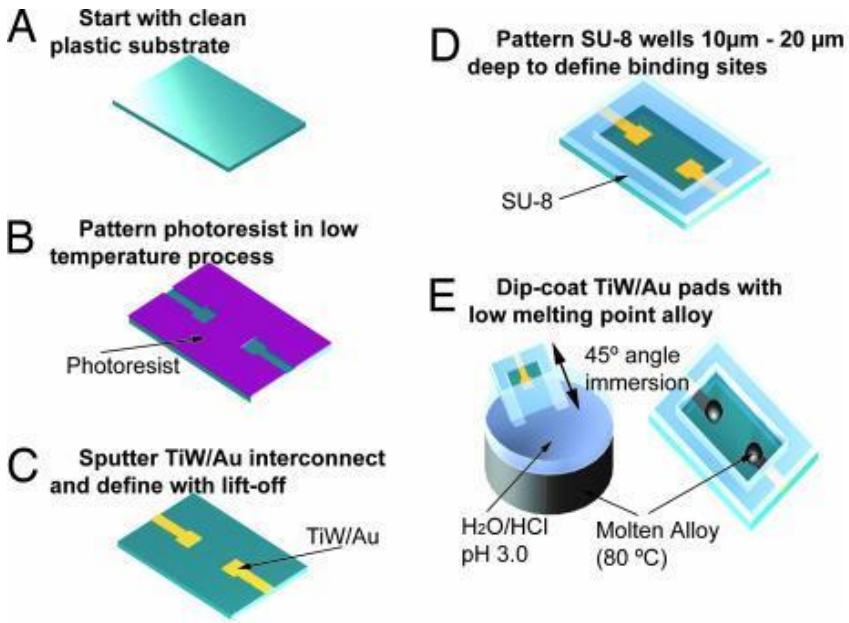

Figure 35 Process flow used to pattern and coat binding sites [31]

After dipping the substrate, each COTS part is dipped in the same bath to coat the contacts. The silicon substrate with Au binding sites is then placed on a hotplate that is set to 65ºC. The individual COTS parts are aligned and attached to create the circuit shown in Figure 36. Two of the binding sites are partially masked with kapton tape to prevent the Au in those regions from being coated with the alloy. Access to the two Au binding sites makes it easier to wirebond the circuit to the thermal initiator on the nanoporous energetic silicon chip.

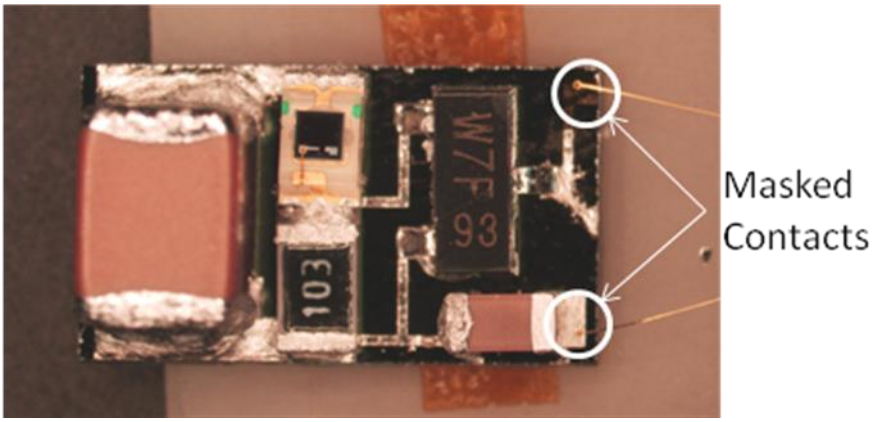

Figure 36 Circuit assembled on Si substrate

The connection between the circuit and the thermal initiator on the nanoporous silicon is made using 127µm aluminum (Al) bond wire. Because this wire is relatively robust, the circuit and the nanoporous energetic silicon can be assembled onto the chassis of the hexapod. Both the circuit on the silicon chip and the nanoporous energetic silicon are attached to the Loctite® chassis using double sided kapton tape. The light detector circuit is attached to the top of the hexapod in Figure 37, while the energetic silicon is attached to the bottom or belly of the hexapod shown in Figure 38.

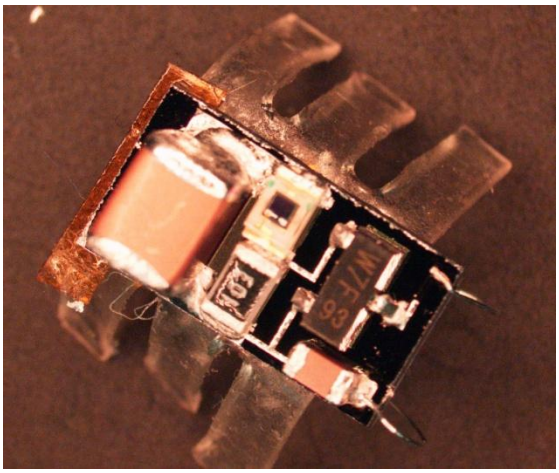

Figure 37 Light detector circuit located on top side of hexapod

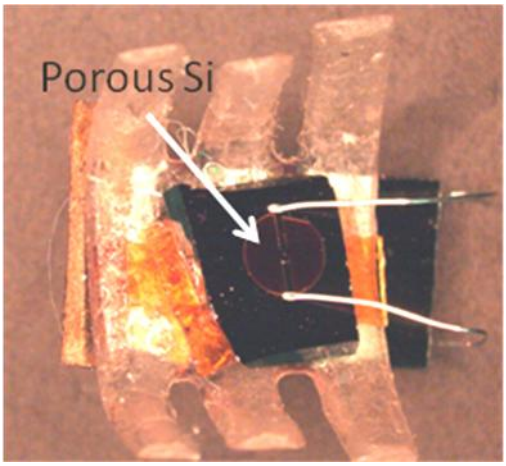

Figure 38 Porous silicon located underneath hexapod

5.2 Integration on Polymers

The use of polymers for integrated circuits has grown rapidly in applications such as identification and product tagging, where platforms are described as low-end high-volume microelectronics [33]. Because polymers offer a structural platform that is both flexible and lightweight, allowing them to be used in organic electronic devices, biomedical devices, and flexible displays [34], they represent an emerging

class of material that can be used for MEMS and nanoelectromechanical systems (NEMS). However, building devices on a micro and nano scale require patterning small feature sizes. This presents a challenge to conventional photolithography techniques used in MEMS fabrication, which require a rigid substrate. Challenges arise with lithographically focusing and handling flexible substrates, and potential adverse "interaction between polymer and developer or other organic solvents used in photolithography" [34]. Polyimide (PI) and polyethyleneterephthalate (PET) are commonly used in making flexible substrates.

Because the goal is to develop a system that can support both electrical and mechanical functionality for a microrobotic platform, there arises the need to pattern metal traces onto flexible substrates, while avoiding delamination and cracking. Both lithographic and non-lithographic techniques for patterning metals on flexible substrates are presented in [35]. A lithographic approach is chosen to pattern metal traces that will serve as the electrical interconnects for the light detector circuit that is integrated onto the hexapod platform.

5.2.1 Hybrid Integration on Flexible Substrate

To eliminate the silicon chip, a hybrid integration technique is demonstrated using a polymer prototyping process developed in [36]. Metal traces can be patterned directly on UV-curable Loctite®3525 that is crafted and cured in the shape of a hexapod in Figure 39. The metal provides binding sites for assembling circuit components. This process is used to fabricate a millimeter scale gripper shown in Figure 40, where actuation is achieved using shape memory alloy [36].

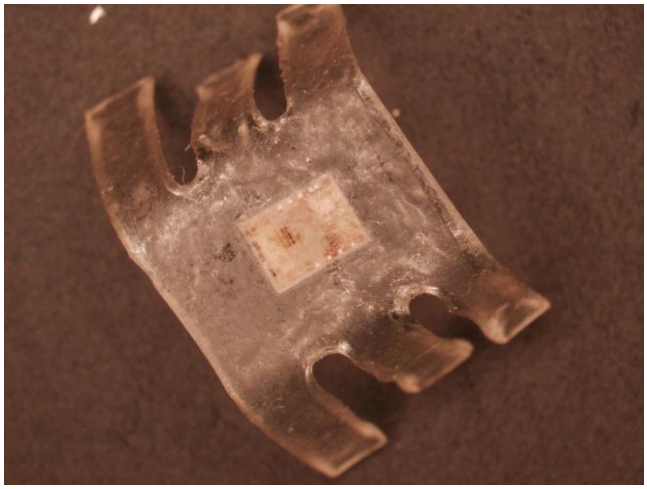

Figure 39 Hexapod made from Loctite polymer

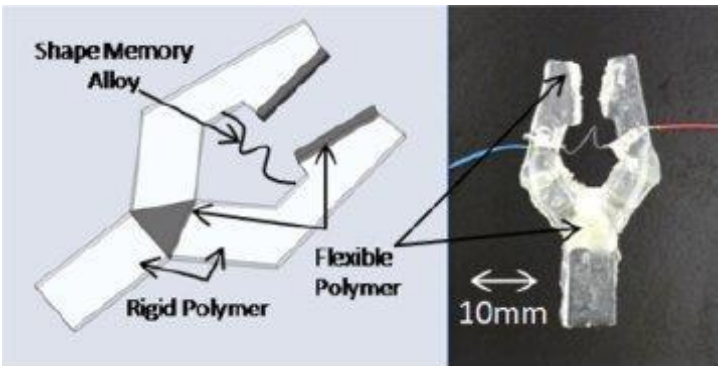

Figure 40 Micro-gripper made from Loctite and actuated with SMA

An initial attempt is made to pattern metal on the Loctite®3525. Similar to patterning photoresist on the LPCVD nitride wafer, a thin layer of the Loctite®3525 is manually spun onto a 4'' silicon wafer and a reverse lithography step is carried out as mentioned above. After developing out the pattern using AZ300, and evaporating Cr and Au, the Loctite®3525 begins to degrade and delaminate from the silicon substrate when placed in PRS-3000 liftoff solution heated to 85ºC. Liftoff in acetone appears to be less aggressive, but results in removal of all the metal features.

After noticing the incompatibilities with the liftoff process, the technique developed in [37] is implemented. While the details of the metal patterning are still to be published, the process involves depositing the polymer onto a transparency sheet, and evaporating a 1μm thick layer of copper once the polymer has been cured. The metal traces are still lithographically defined, but the copper is protected in specific regions on the polymer substrate with a photoresist mask. Once the resist is developed, exposed copper (Cu) is then removed using a mixture of nitric acid and water. Figure 41, shows a hexapod platform made using UV cured Loctite®3525. "U" shaped metal traces have been patterned on each leg of the hexapod. The processing technique has been refined to avoid the apparent cracks in the Cu layer.

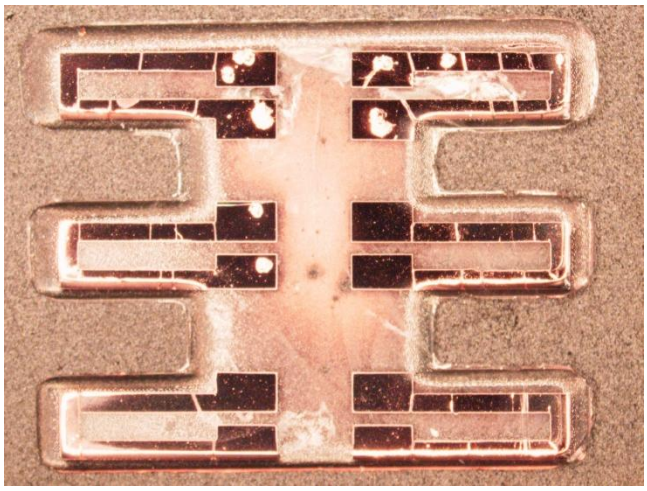

Figure 41 Hexapod with evaporated Cu traces

5.2.2 Circuit Assembly on Flexible Substrate

The silicon chip is removed from the top of the hexapod, and the circuit assembled directly onto the polymer substrate. Once metal traces are patterned using the approach developed in [37], we apply the solder dipping process mentioned above. Because the Loctite®3525 should be stored below 100ºC, the molten alloy

dipping process is modified to avoid damaging the polymer. The temperature of the ethylene glycol and In-Bi-Sn-Pb-Cd is reduced to 65ºC. Maintaining a bath temperature of 80ºC, which is used to dip the silicon chip, causes deformation of the polymer. The hexapod is submerged in the heated ethylene glycol and In-Sn-Pb-Cd solution for approximately 10 seconds and removed. The hexapod is momentarily submerged in a beaker filled with H_20, upon removal from the ethylene glycol solution. The copper traces are successfully coated with the In-Sn-Pb-Cd alloy. Surface mount components, including two 10kΩ resistors and a phototransistor are dipped in the alloy to coat their metal contacts. The polymer hexapod is then placed on a hotplate set to 65ºC, and the circuit components are attached using a pair of tweezers. Pressure is applied between the component and the binding site to ensure a robust connection. The sample hexapod is then removed from the hotplate and allowed to cool. As the polymer substrate cools, the circuit components are fused to the binding sites. Figure 42 shows attachment of surface mount components to the hexapod.

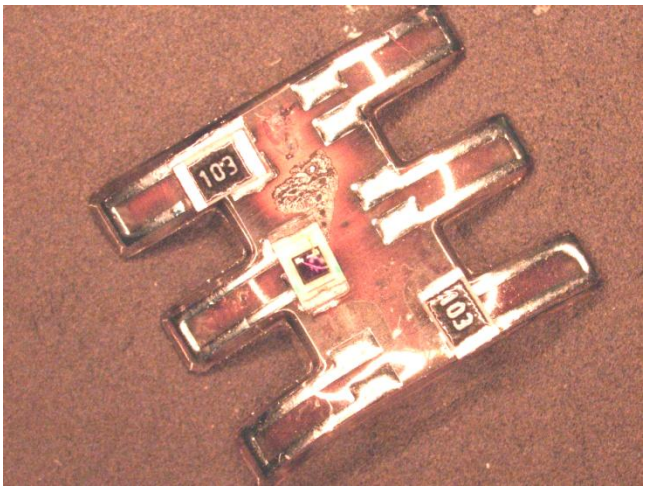

Figure 42 Surface mount resistors attached to hexapod chassis using low temperature alloy

While this technique proves effective for attaching three relatively small surface mount components, integrating the proposed light sensing circuit is not trivial. The metal electrical traces for the circuit are successfully transferred to the polymer, and the polymer is dipped in the molten alloy. The components are dip coated and attached to the hexapod as shown in Figure 43. After the hexapod and the circuit components are allowed to cool, the electrical traces become extremely brittle when the legs of the hexapod are flexed.

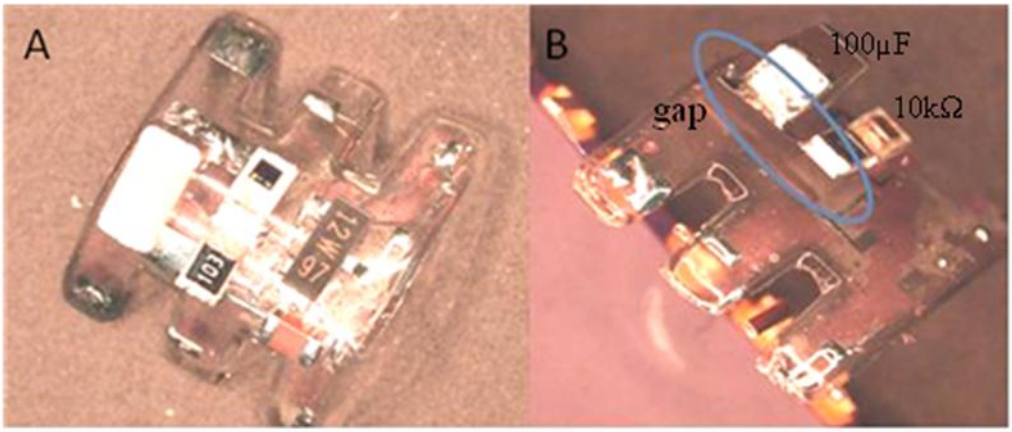

Figure 43 (A) Circuit attached directly to hexapod chassis (B) Delamination of metal traces when polymer flexed

While the microrobot appears to be attached to the polymer chassis in Figure 43, closer observation shows that the 100μF capacitor and the 10kΩ resistor have detached from the polymer. While still attached to the underlying Cu trace and alloy, it appears that delamination is occurring at the point where the polymer material is being strained, which introduces stress in the film. The polymer is strained to position the leg out of plane. The behavior is potentially the result of thermally induced stress. Prior to dip coating the hexapod, the structure can undergo moderate flexing without delaminating, although some cracking occurs. After dip coating the

polymer at 65°C, the hexapod is dipped in a beaker of room temperature water to rinse the ethylene glycol. This rapid temperature change could potentially cause weakening at the polymer-metal interface, with possible contraction of the film.

Such behavior is common in polymers when their temperature drops below the glass transistor temperature, T_g. Below T_g the polymer becomes brittle, while at temperatures above T_g, the polymer becomes more rubber-like. Processing polymers between the T_g regime and the freezing temperature regime is critical to maintain structural integrity. Therefore, to avoid delamination of the metal traces, the polymer is pre-stressed prior to solder dipping. The underside of the chassis is coated with a thin layer of Loctite, which is then cured, allowing the legs to maintain their form.

In addition to delamination of the metal trace, stress applied to the hexapod joints results in cracking of the electrical traces. For lithographically defined features below 133µm, cracks in the copper layer are unnoticeable to the naked eye. Once the hexapod is dip coated with the low temperature alloy, the cracks widen, resulting in an open circuit. A number of cracks are shown in Figure 44. This 133µm wide trace connects the FET and capacitor to ground. For wider electrical traces measuring 415µm in width, the effect of cracking in the underlying copper is negligible. Because the contact area is larger, better wetting of the alloy causes the cracks to be filled. Therefore to eliminate potential electrical discontinuity, the minimum feature size is increased from 133µm to 415µm.

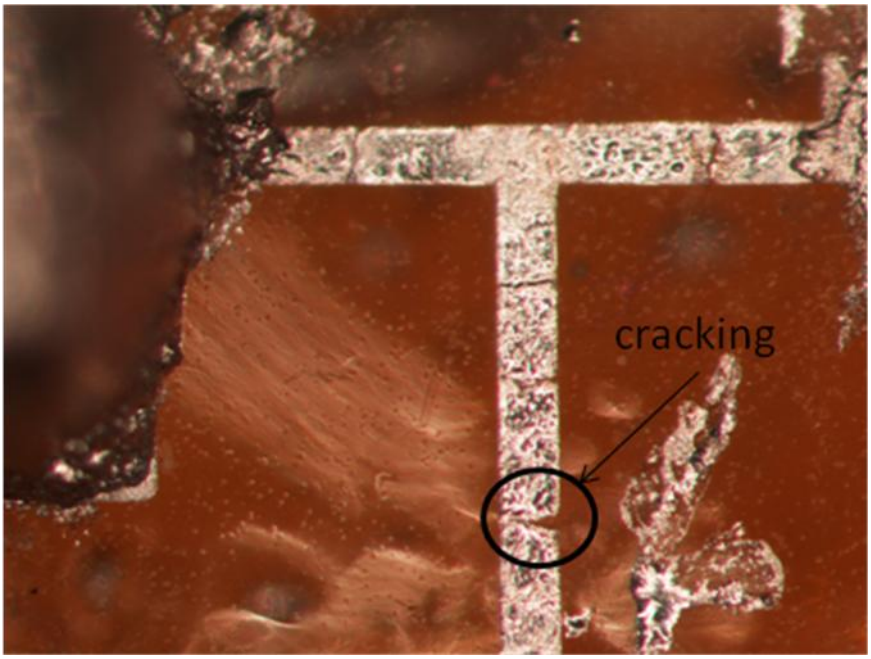

Figure 44 Cracking in metal electrical traces

5.3 Integration of Nanoporous Energetic Silicon

Once the on-board power supply and sensor have been integrated onto the polymer chassis, electrical connection is made between the circuit and the nanoporous energetic silicon by manually soldering thin wires from the capacitor and FET to contact pads situated on the nanoporous energetic silicon sample. Figure 45 shows a top-down view of a fully integrated hexapod where wires have been soldered to the drain of the FET and the capacitor used to supply power to initiate the energetic. The wires are soldered prior to assembling the components onto the polymer chassis.

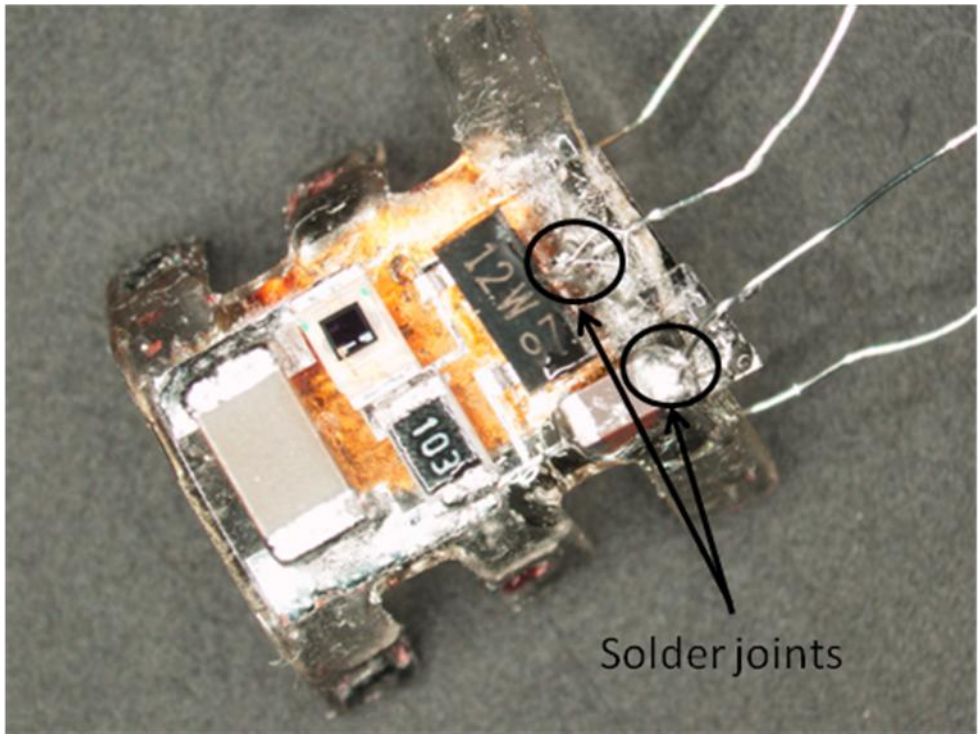

Figure 45 Solder joints made directly to FET and capacitor before assembling circuit on hexapod

To solder to the nanoporous energetic silicon Loctite is used as an adhesive to fix two metallic pads to the silicon substrate. These pads, shown in Figure 46, are aligned adjacent to the initiator wire on the porous silicon material. Connection between the initiator wire and the pads are made using a 25.4µm Au wire bond. The capacitor and FET are then soldered to the pads. The energetic chip is then stuck to the underside of the hexpod using double sided kapton tape.

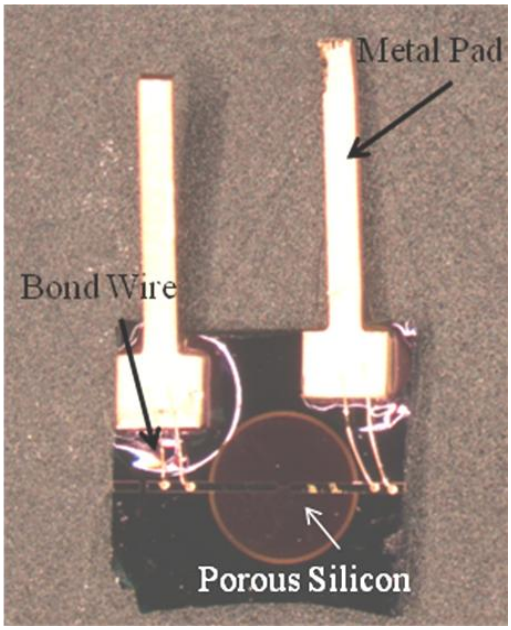

Figure 46 Metal pads attached to energetic chip using Loctite

After attaching the nanoporous energetic silicon to the underside of the hexapod, wires are soldered to the pads connecting the circuit to the initiator on the nanoporous silicon shown in Figure 47. Oxidizer is then applied to the nanoprous silicon and allowed to dry.

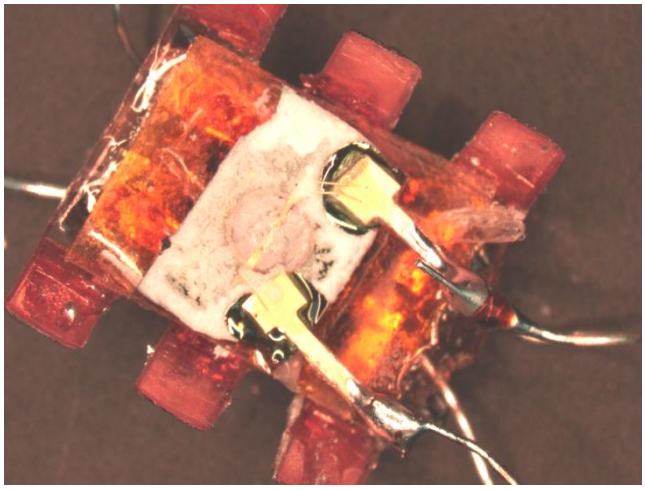

Figure 47 Circuit connected to oxidized nanoporous Si by soldering to pads on the substrate

This new hybrid integration process allows the polymer to be used as a structural chassis for the direct assembly of a circuit, which interfaces with a chemical actuator. The overall mass of the robotic platform can potentially be reduced by eliminating the rigid silicon chip. While rigidity of the substrate is important in most MEMS micromachining processes, this hybrid integration allows for micron scale features to be lithographically defined and patterned. These can be used as electrical traces for attaching circuit components or integration of various actuators.

Chapter 6: Experimentation

Analysis of the fully integrated platform is done by measuring the vertical distance traveled by the sub-cubic centimeter microrobot when it senses a change in light intensity. The lighting conditions are varied from an illuminance of 0.27 lux, which is comparable to a full moon on a clear night [38], to approximately 26.21 lux, which is less that the illuminance of a family living room [38]. Using a 3 LED array having a luminous output of 750 total lumens, the area over which the flux is spread is taken into consideration to determine the perceived lighting conditions. Experimental results are based on charging up the circuit in a dark environment, and then illuminating the microrobot to actuate the jumping mechanism. These results are gathered for two separate microrobotic platforms. For the first platform, the circuit is assembled on a silicon substrate then attached to the hexapod as discussed in Chapter 5. The circuit is assembled directly onto the polymer chassis in the second platform.

6.1 Electrical Characterization

Before demonstrating jumping of the microrobot, a simple experiment is run to determine the leakage voltage of the capacitor when isolated from the circuit. This test is independent of the capacitor discharge discussed in Chapter 4, where a capacitor switch test is performed. The discharge time of the 10μF capacitor is analyzed, because it must supply 5VDC to the thermal initiator once it is connected through the switching FET. Leads are soldered to a 10 μF, 16V surface mount capacitor and the capacitor is inserted into a breadboard. Completely isolated, the capacitor is subjected to ambient atmospheric conditions, with a relative humidity of

48%. Charged up to 6V, there appears to be a rapid decay in the voltage over the first 2.5 hours, over which the voltage drops below 5V, which is shown in Figure 48.

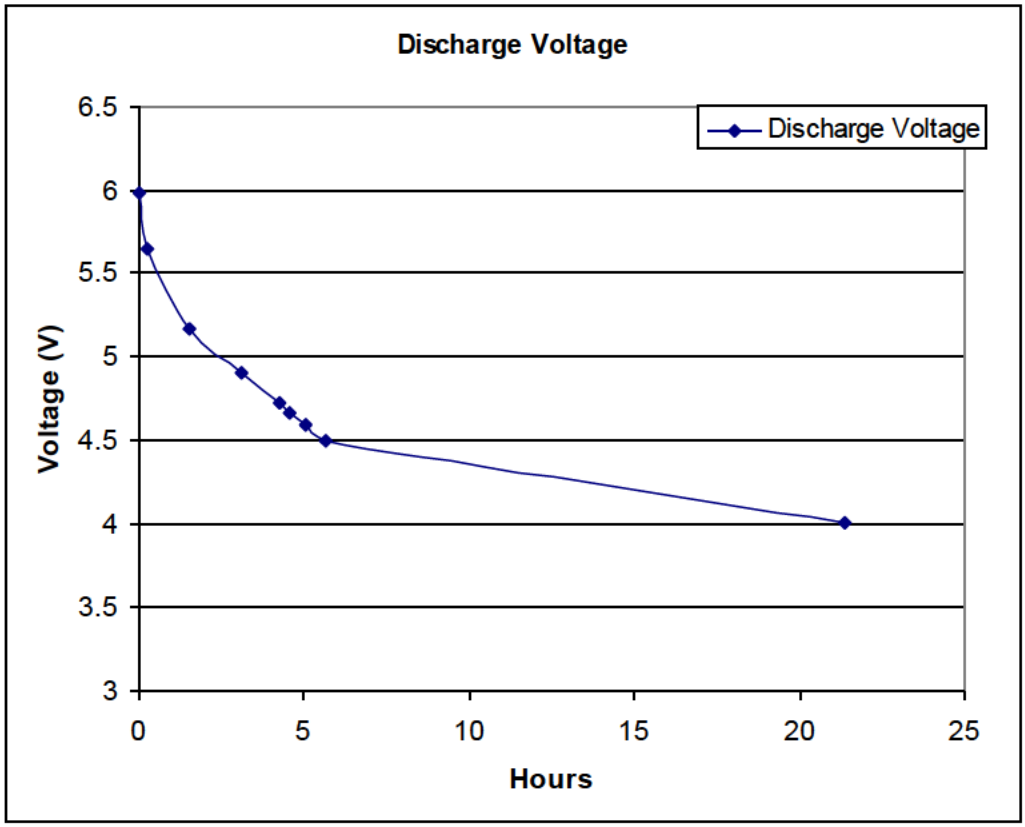

Figure 48 Capacitor discharge voltage as a function of time

The full circuit is then assembled on a 4mm by 7mm silicon chip. The 100µF and 10µF capacitors are charged to 6VDC. After charging the capacitors, the circuit is left in a dark environment for 8 minutes before triggering the phototransistor with a light source. This is done to determine how long the capacitors can maintain sufficient voltage for the circuit to sense and actuate. The current across the initiator is shown in Figure 49 after 8 minutes of elapsed time. After 8 minutes, the circuit

supplies approximately 500mA of current. This is sufficient to ignite the nanoporous energetic material.

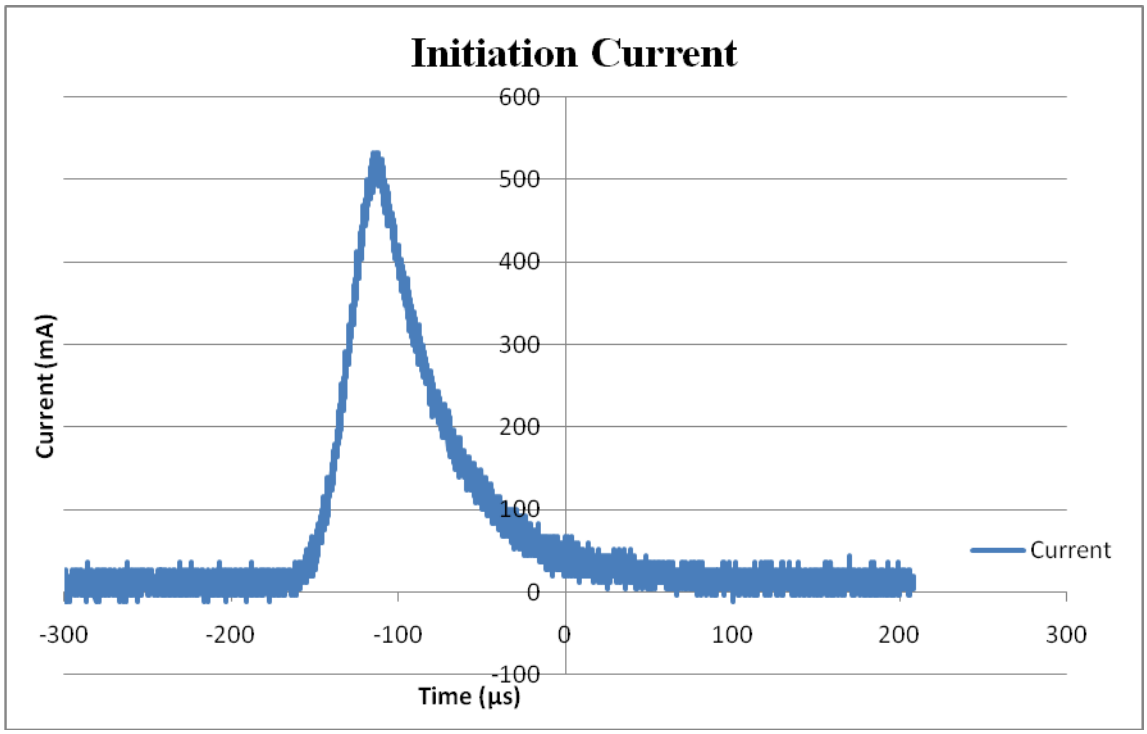

Figure 49 Current across initiator after capacitor is charged for 8 minutes

6.2 Jumping Micro-Robot

6.2.1 Hybrid Integration on Silicon

To demonstrate jumping locomotion using hybrid integration on silicon, the circuit is assembled on a silicon-silicon nitride substrate and attached to the top of the microrobot with double-sided kapton tape. A 2mm diameter, 75-82µm deep, nanoporous energetic silicon sample is attached to the underside of the hexapod using double-sided kapton tape. Electrical connection is made between the circuit and the energetic material using a pair of 127µm aluminum wirebonds. Figure 50 shows the

assembled control circuit attached to the porous silicon chip via wirebonds. Table 9 provides a breakdown of the mass of the system. With a mass of 338mg, which includes the circuit, and hexapod chassis; the 100µF capacitor accounts for nearly half the mass of the entire system.

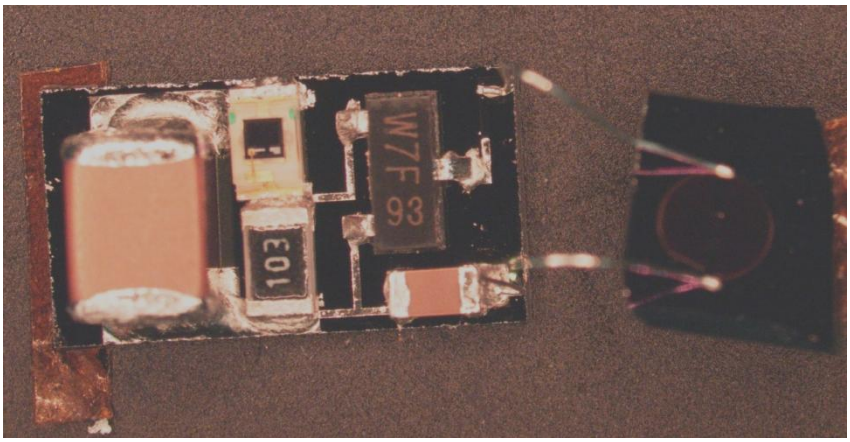

Figure 50 Circuit assembled on Si substrate and connected to nanoprous silicon

Component	Mass (mg)
Si substrate	74
10µF capacitor	8.7
100µF capacitor	131.3
2N7002 FET	8.4
SFH3710	3.3
10kΩ resistor	4.5
Hexapod	69.8
Energetic chip	38.6
Total Mass	338.6

Table 9 Mass of individual components used to assemble hexapod on Si

The experiment is run by first charging the two capacitors in a darkened room to prevent the phototransistor from leaking. Once charged, the jump is triggered by illuminating the phototransistor using a set of 3 high-intensity LEDs. The event is captured at 1000 frames per second using a high speed camera.

A maximum height of 6 cm, shown in Figure 51, is achieved when the energetic material is ignited. The microrobot flips approximately 20 revolutions per second during the jump. This rotational behavior is due to the unbalanced weight distribution resulting from the 100µF capacitor being positioned at the edge of the microrobot. Based on estimates for rotation axis and moment of inertia, the calculated rotational energy is approximately 32µJ, which is about 16% of the total kinetic energy. The total kinetic energy is 199µJ.

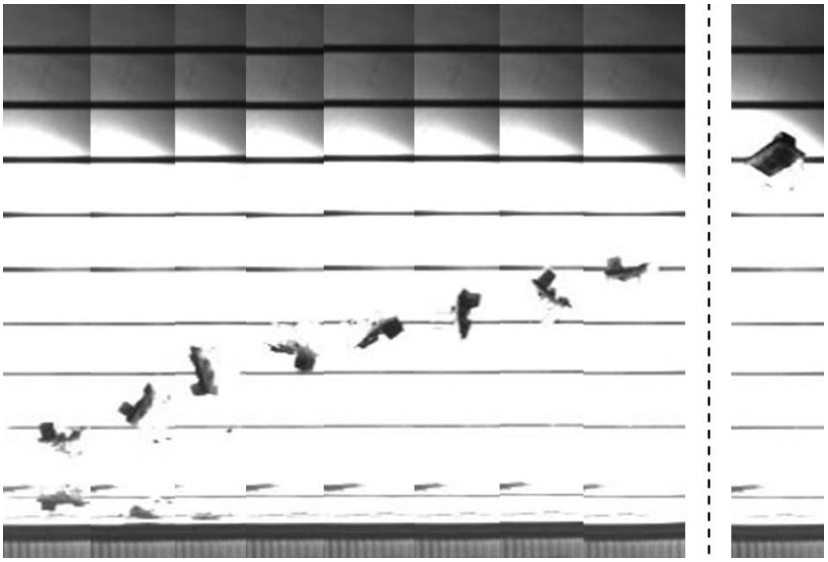

Figure 51 Successive frames showing 6cm jump of hexapod with circuit assembled on Si substrate

6.2.2 Hybrid Integration on Loctite

The control circuit is assembled directly onto the Loctite chassis using the low temperature alloy dipping process discussed in Chapter 5. The hexapod and circuit components are separately coated with the alloy, and wires are soldered to the capacitors before the hexapod is assembled on a hotplate. Table 10 shows the mass

for each component. The mass of the chip is approximately 38.6mg. The actual mass of the energetic porous silicon is 0.21mg, indicating that less than 1% of the mass of the chip is due to the actual energetic porous silicon material. Once the hexapod has been assembled, the circuit and underlying electrical traces are coated with an additional layer of Loctite. This additional layer of Loctite is important because it enhances the adhesion between the metal electrical traces and the underlying polymer by eliminating potential delamination. The polymer microrobot is slightly lighter than the hexapod used to demonstrate the 6cm jump. This robust integration allows for hexapod legs to be flexed and potentially actuated out of plane, without disturbing the functionality of the circuit.

Component	Mass (mg)
10µF capacitor	8.7
100µF capacitor	131.3
2N7002 FET	8.4
SFH3710	3.3
10kΩ resistor	4.5
Hexapod with Wires and Loctite	111.8
Gold Connectors	7.4
Energetic Chip	38.6
Total Mass	314

Table 10 Mass of individual components used to assemble hexapod on polymer chassis

The initial experiment to demonstrate a jump using the hybrid integration on a silicon substrate is conducted under relatively low humidity conditions. Relative humidity below 20% is critical to achieving a stronger exothermic reaction, which results in higher energy output and thrust. The sodium perchlorate that is applied to the porous silicon to make it energetic is hygroscopic, and shows a strong tendency to absorb

moisture over time. As the oxidizer attracts water molecules, stress induced in the pores leads to cracking of the porous layer. Over time, this causes failure of the integrated initiator. At 50% humidity, the resistance of the initiator degrades from an optimal resistance of 3.2Ω to greater than 4MΩ. At 4MΩ, the control circuit is unable to supply sufficient current to ignite the energetic porous silicon. Although experiments are carried out in a dry box plumbed with nitrogen, the process of opening the door to charge the capacitors prior to ignition provides enough time (1min) for the oxidizer to take on water.

A number of techniques are employed to limit the rate at which moisture is absorbed by the oxidizer once applied to the pores. The first technique involves applying 1 drop of oxidizer using a 3cc/mL syringe in a dry room and allowing the sample to dry for 20 minutes. After the sample is dry, a thin layer of Loctite is carefully applied on top of the porous silicon and UV cured for 5 minutes. The sample can be transported from the dry room and soldered to the control circuit, without degrading the initiator. The porous silicon is successfully ignited at relative humidity of 50%. A vertical jump distance of 1cm achieved by this 280mg hexapod is limited by the Loctite, which creates a thin coating around the energetic material. A portion of output energy being converted into thrust for movement is lost to breaking the seal created by the Loctite. As an alternative to the Loctite, the porous silicon is sealed with parylene, but no significant improvements in the jump height are observed. In attempting to load the sample into the parylene system, the exposure to moisture is not minimized. Although the samples are dried in a nitrogen dry box, taking several minutes to transport the samples to the parylene system is enough to

induce cracking. An alternative approach is to dry the sample under a nitrogen stream generated by the parylene system to avoid transport.

A significant jump height of 8cm, shown in Figure 52, is achieved without sealing the nanoporous energetic silicon with Loctite or parylene, allowing us to avoid loss of energy needed to break the seal. For this experiment a small dry box is filled with a continuous stream of nitrogen. Leads from an external power supply are fed into the box. With the leads connected to the hexapod, the oxidizer is applied and the box sealed for 15 minutes. After the oxidizer is dry, the door is then opened for less than 30 seconds to disconnect the leads. The door is then closed to minimize moisture entering the box. The light source positioned above the enclosure is turned on, triggering ignition of the energetic nanoporous silicon.

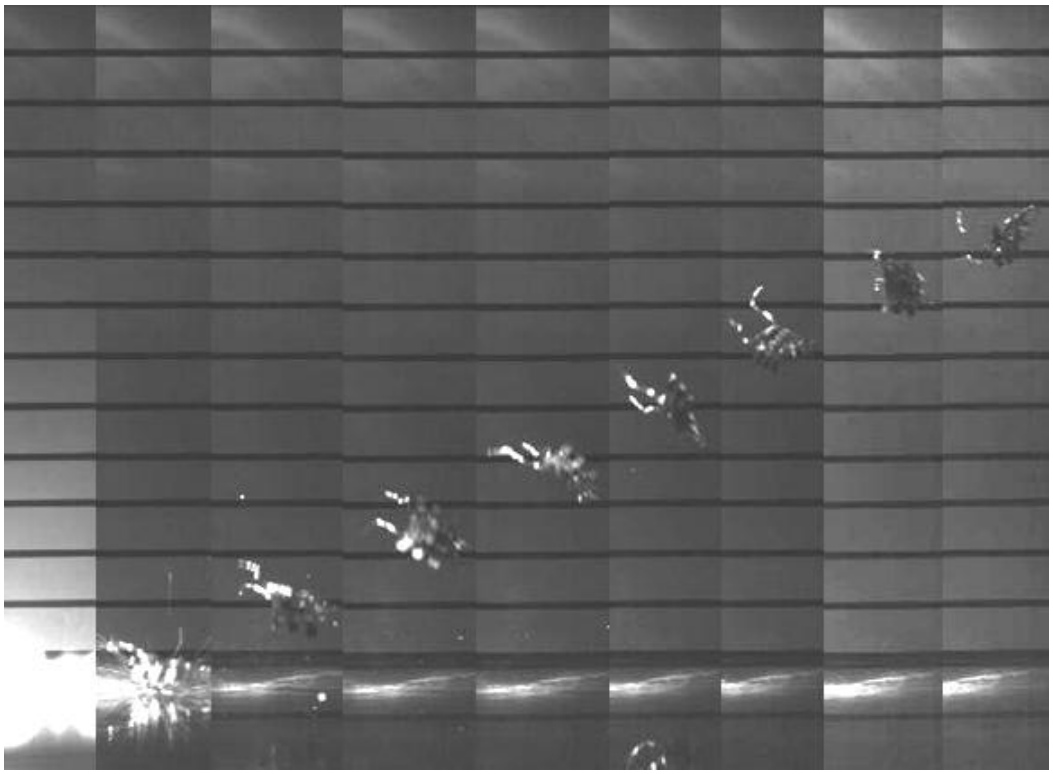

Figure 52 Successive frames showing 8cm jump of hexapod with circuit assembled on polymer chassis

High speed video of the jump is captured at 1000 frames per second. Based on the distance and time of flight, the translational kinetic energy of the hexapod is 246μJ. The center of gravity is calculated for the composite body by measuring the distance of separation of the circuit components on the chassis with respect to a common axis dissecting the large 100μF capacitor. Using the value calculated for the distance to the axis of rotation, and the solving for the moment of inertia based on a thin plate approximation for the hexapod, the rotational kinetic energy is 3.2μJ for the jumping hexapod.

Chapter 7: Conclusions and Future Work

7.1 Conclusions

The first-ever autonomous jumping microrobot has been demonstrated, achieving a vertical jump height of 8cm. Autonomy is achieved through on-board optical sensing, which allows the hexapod to detect a change in light intensity. In addition, the use of a novel energetic material for actuation is shown, where relatively low input energy is required to propel a 314mg mass 8cm in the air. The 0.21mg, 2mm diameter energetic is able to propel an object more than 1000 times its mass, 8cm into the air. In achieving jumping locomotion, 3.2μJ of rotational kinetic energy and 246μJ of translational kinetic energy is generated from the reaction output

A modified hybrid integration approach is developed, which allows for the direct integration of a control circuit on a flexible substrate using a low temperature alloy dipping process, eliminating the need to use a silicon substrate to assemble electronics onto the chassis of the microrobot. In the first hybrid approach, the control circuit is assembled on a silicon chip fixed to the polymer hexapod. The second approach involves reducing the mass of the hexapod by eliminating the silicon substrate for direct integration onto the flexible substrate. The 2cm increase in vertical jump height is a lower bound for a considerably larger jump height that could be achieved if the energetic output is increased and the energy is focused to enhance directionality.

7.2 Future Work

To further improve on the hybrid integration approach demonstrated in this thesis, there is a critical need to eliminate manual soldering and wirebonding to make direct connections from the control circuit on the hexapod to the energetic material. To accomplish this, implementation of vias in the polymer chassis is necessary. Introducing vias into the design would allow for assembling electrical components on the top and bottom of the chassis by making electrical connections through the flexible substrate material. The via walls could be electroplated and filled with the low temperature alloy for low contact resistance.

While the energetic material used to actuate the microrobot platform has a limited jump cycle, there are a number of potential applications that can be realized using nanoporous silicon that offers a unique alternative to traditional energetics. Future work would involve pursing applications that might be more suited for one-time jumping. These may include tracking and reconnaissance, where the energetic can be used for placing and positioning electronic devices in strategic positions to acquire sensitive data. Harnessing the thruster capability and energetic output, this material could be used for electronically controlled thrusters that could be integrated alongside any number of sensors and actuators. Potential applications exist where the energetic material could be integrated alongside sensor nodes and deployed on the battlefield. In rough, dense terrain that may impede RF communication, limited jumping could prove a useful approach to sending and receiving packets of information, or to deploy an antenna once the platform has reached its destination, reducing the size and increasing the stealth of the device on the battlefield.

In addition to potential applications for the energetic material, possible alternatives to packaging the energetic material to make it less susceptible to moisture could be explored. This would involve exploring new materials, in addition to Loctite and parylene, to seal out moisture to increase the longevity and utility of the device. Finally, it would be advantageous to develop polymer based switches or MEMS switches that can be integrated onto the polymer chassis to isolate capacitors. This could potentially reduce leakage and allow the circuit to maintain sufficient voltage over a longer period of time.

Bibliography

[1] Siegel, M.;, "Smart sensors and small robots," *Instrumentation and Measurement Technology Conference, 2001. IMTC 2001. Proceedings of the 18th IEEE* , vol.1, no., pp.303-308 vol.1, 21-23 May 2001
doi: 10.1109/IMTC.2001.928830
URL: http://ieeexplore.ieee.org/stamp/stamp.jsp?tp=&arnumber=928830&isnumber=20066

[2] Donald, B.R.; Levey, C.G.; McGray, C.D.; Paprotny, I.; Rus, D.;, "An untethered, electrostatic, globally controllable MEMS micro-robot," *Microelectromechanical Systems, Journal of* , vol.15, no.1, pp. 1- 15, Feb. 2006
doi: 10.1109/JMEMS.2005.863697
URL: http://ieeexplore.ieee.org/stamp/stamp.jsp?tp=&arnumber=1588903&isnumber=33485

[3] Casanova, R.; Dieguez, A.; Arbat, A.; Alonso, O.; Sanuy, A.; Canals, J.; Colomer, J.; Samitier, J.;, "Integration of the control electronics for a mm^3-sized autonomous microrobot into a single chip," *Robotics and Automation, 2009. ICRA '09. IEEE International Conference on* , vol., no., pp.3007-3012, 12-17 May 2009
doi: 10.1109/ROBOT.2009.5152611
URL: http://ieeexplore.ieee.org/stamp/stamp.jsp?tp=&arnumber=5152611&isnumber=5152175

[4] Fiorini, P.; Hayati, S.; Heverly, M.; Gensler, J.;, "A hopping robot for planetary exploration," *Aerospace Conference, 1999. Proceedings. 1999 IEEE* , vol.2, no., pp.153-158 vol.2, 1999
doi: 10.1109/AERO.1999.793156
URL: http://ieeexplore.ieee.org/stamp/stamp.jsp?tp=&arnumber=793156&isnumber=17211

[5] Tsukagoshi, H.; Sasaki, M.; Kitagawa, A.; Tanaka, T.;, "Design of a Higher Jumping Rescue Robot with the Optimized Pneumatic Drive," *Robotics and Automation, 2005. ICRA 2005. Proceedings of the 2005 IEEE International Conference on* , vol., no., pp. 1276- 1283, 18-22 April 2005
URL: http://ieeexplore.ieee.org/stamp/stamp.jsp?tp=&arnumber=1570291&isnumber=33250

[6] Wikipedia contributors, "Robot Locomotion," *Wikipedia, The Free Encyclopedia*. Wikipedia, The Free Encyclopedia, 23 Mar 2010. Web. 16 Apr 2010
URL: http://en.wikipedia.org/wiki/Robot_locomotion

[7] Ebefors, T.; Mattsson, T.; Kalvesten, E.; Stemme, G.;, "A Walking Silicon Micro-Robot," *The 10th Int. Conference on Solid-State Sensors and Actuators (Transducers'99)*, Sendai, Japan, pp. 1202-1205, 7-10 June 1999

[8] Lambrecht, B.G.A.; Horchler, A.D.; Quinn, R.D.;, "A Small, Insect-Inspired Robot that Runs and Jumps," *Robotics and Automation, 2005. ICRA 2005. Proceedings of the 2005 IEEE International Conference on* , vol., no., pp. 1240-1245, 18-22 April 2005
URL: http://ieeexplore.ieee.org/stamp/stamp.jsp?tp=&arnumber=1570285&isnumber=33250

[9] Stoeter, S.A.; Rybski, P.E.; Gini, M.; Papanikolopoulos, N.;, "Autonomous stair-hopping with Scout robots," *Intelligent Robots and Systems, 2002. IEEE/RSJ International Conference on*, vol.1, no., pp. 721- 726 vol.1, 2002
doi: 10.1109/IRDS.2002.1041476
URL: http://ieeexplore.ieee.org/stamp/stamp.jsp?tp=&arnumber=1041476&isnumber=22324

[10] Armour, R.; Paskins, K; Bowyer, A.; Vincent, J; Megill, W;, "Jumping robots: a biomimetic solution to locomotion across rough terrain," Bioinspiration and Biomimetics, IOP Publishing, vol.2, no., pp.S65-S82, 2007
Doi: 10.1088/1748-3182/2/3/S01
URL: stacks.iop.org/BB/2/S65

[11] Center for Distributed Robotics, University of Minnesota, "Scout Robot," [Online]. Available: http://distrob.cs.umn.edu/robots/scout/Scout_2k_View_1.jpg. [Accessed: May 22, 2010]

[12] Wikipedia contributors, "Fantastic Voyage." *Wikipedia, The Free Encyclopedia*. Wikipedia, The Free Encyclopedia, 10 Aug. 2008. Web. 16 Apr. 2010
URL: http://en.wikipedia.org/wiki/Fantastic_voyage

[13] Hoover, A.M.; Steltz, E.; Fearing, R.S.; , "RoACH: An autonomous 2.4g crawling hexapod robot," *Intelligent Robots and Systems, 2008. IROS 2008. IEEE/RSJ International Conference on*, vol., no., pp.26-33, 22-26 Sept. 2008
doi: 10.1109/IROS.2008.4651149
URL: http://ieeexplore.ieee.org/stamp/stamp.jsp?tp=&arnumber=4651149&isnumber=4650570

[14] Kovac, M.; Fuchs, M.; Guignard, A.; Zufferey, J.-C.; Floreano, D.; , "A miniature 7g jumping robot," *Robotics and Automation, 2008. ICRA 2008. IEEE International Conference on* , vol., no., pp.373-378, 19-23 May 2008
doi: 10.1109/ROBOT.2008.4543236
URL: http://ieeexplore.ieee.org/stamp/stamp.jsp?tp=&arnumber=4543236&isnumber=4543169

[15] Woern, H.; Szymanski, M.; Seyfried, J.; , "The I-SWARM project," *Robot and Human Interactive Communication, 2006. ROMAN 2006. The 15th IEEE International Symposium on* , vol., no., pp.492-496, 6-8 Sept. 2006
doi: 10.1109/ROMAN.2006.314376
URL: http://ieeexplore.ieee.org/stamp/stamp.jsp?tp=&arnumber=4107855&isnumber=4107769

[16] Fei Li; Bonsignori, G.; Scarfogliero, U.; Dajing Chen; Stefanini, C.; Weiting Liu; Dario, P.; Xin Fu; , "Jumping mini-robot with bio-inspired legs," *Robotics and Biomimetics, 2008. ROBIO 2008. IEEE International Conference on* , vol., no., pp.933-938, 22-25 Feb. 2009
doi: 10.1109/ROBIO.2009.4913124
URL: http://ieeexplore.ieee.org/stamp/stamp.jsp?tp=&arnumber=4913124&isnumber=4912969

[17] Laksanacharoen, S.; Pollack, A.J.; Nelson, G.M.; Quinn, R.D.; Ritzmann, R.E.; , "Biomechanics and simulation of cricket for microrobot design," *Robotics and Automation, 2000. Proceedings. ICRA '00. IEEE International Conference on* , vol.2, no., pp.1088-1094 vol.2, 2000
doi: 10.1109/ROBOT.2000.844744
URL: http://ieeexplore.ieee.org/stamp/stamp.jsp?tp=&arnumber=844744&isnumber=18246

[18] Wikipedia contributors, “Drag coefficient.” *Wikipedia, The Free Encyclopedia*. Wikipedia, The Free Encyclopedia, 26 May. 2010. Web. 1 June. 2010
URL: http://en.wikipedia.org/wiki/Drag_coefficient

[19] Scarfogliero, U.; Stefanini, C.; Dario, P.; , "Design and Development of the Long-Jumping "Grillo" Mini Robot," *Robotics and Automation, 2007 IEEE International Conference on* , vol., no., pp.467-472, 10-14 April 2007
doi: 10.1109/ROBOT.2007.363830
URL: http://ieeexplore.ieee.org/stamp/stamp.jsp?tp=&arnumber=4209135&isnumber=4209049

[20] Birch, M.C.; Quinn, R.D.; Hahm, G.; Phillips, S.M.; Drennan, B.; Fife, A.; Verma, H.; Beer, R.D.; , "Design of a cricket microrobot," *Robotics and Automation, 2000. Proceedings. ICRA '00. IEEE International Conference on* , vol.2, no., pp.1109-1114 vol.2, 2000
doi: 10.1109/ROBOT.2000.844747
URL: http://ieeexplore.ieee.org/stamp/stamp.jsp?tp=&arnumber=844747&isnumber=18246

[21] Bergbreiter, S.; Pister, K.S.J.; , "Design of an Autonomous Jumping Microrobot," *Robotics and Automation, 2007 IEEE International Conference on* , vol., no., pp.447-453, 10-14 April 2007
doi: 10.1109/ROBOT.2007.363827
URL: http://ieeexplore.ieee.org/stamp/stamp.jsp?tp=&arnumber=4209132&isnumber=4209049

[22] Lewis, D.H., Jr.; Janson, S.W.; Cohen, R.B.; Antonsson, E.K.; , "Digital MicroPropulsion," *Micro Electro Mechanical Systems, 1999. MEMS '99. Twelfth IEEE International Conference on* , vol., no., pp.517-522, 17-21 Jan 1999
doi: 10.1109/MEMSYS.1999.746882
URL: http://ieeexplore.ieee.org/stamp/stamp.jsp?tp=&arnumber=746882&isnumber=16111

[23] K. Zhang, S.K. Chou, S.S. Ang, X.S. Tang, "A MEMS-based solid propellant microthruster with Au/Ti Igniter," *Sensors and Actuators*, vol.122, no.1, pp.113-123, 29, July 2005

[24] Shende, R., et al., *Nanostructured Energetic Materials, Session M,*. 25th Army Science Conference, Orlando, Fl., 2006.

[25] Churaman, W.; Currano, L.; Becker, C.; "Initiation and reaction tuning of nanoporous energetic silicon," *Journal of Physics and Chemistry of Solids. EMRS 2009 Symposium D: Nano-scale Energetic Materials: Fabrication, Characterization and Molecular Modeling - EMRS 2009 Symposium DS,* vol.71, no.2, pp.69-74, February 2010

[26] Curdaneli, S.; Ak, M.A.; Ulas, A.; , "Experimental Analysis on the Measurement of Ballistic Properties of Solid Propellants," *Recent Advances in Space Technologies, 2007. RAST '07. 3rd International Conference on* , vol., no., pp.231-235, 14-16 June 2007
doi: 10.1109/RAST.2007.4283983
URL: http://ieeexplore.ieee.org/stamp/stamp.jsp?tp=&arnumber=4283983&isnumber=4283956

[27] Currano, L.; Churaman, W.; Becker, C.; , "Nanoporous silicon as a bulk energetic material," *Solid-State Sensors, Actuators and Microsystems Conference, 2009. TRANSDUCERS 2009. International* , vol., no., pp.2172-2175, 21-25 June 2009
doi: 10.1109/SENSOR.2009.5285607
URL: http://ieeexplore.ieee.org/stamp/stamp.jsp?tp=&arnumber=5285607&isnumber=5285368

[28] Currano, L.J.; Churaman, W.A.; , "Energetic Nanoporous Silicon Devices," *Microelectromechanical Systems, Journal of* , vol.18, no.4, pp.799-807, Aug. 2009
doi: 10.1109/JMEMS.2009.2023883
URL: http://ieeexplore.ieee.org/stamp/stamp.jsp?tp=&arnumber=5129692&isnumber=5185350

[29] P. W. Cooper and S. R. Kurowski, *Introduction to the Technology of Explosives*, Wiley-VCH, NJ, 1996.

[30] Xu, Y.; Tai, Y.C.; Huang, A.; Ho, C.; , "IC-integrated flexible shear-stress sensor skin," *Microelectromechanical Systems, Journal of* , vol.12, no.5, pp. 740-747, Oct. 2003
doi: 10.1109/JMEMS.2003.815831
URL: http://ieeexplore.ieee.org/stamp/stamp.jsp?tp=&arnumber=1240146&isnumber=27805

[31] Morris, C.; Parviz, B.;, "Micro-scale metal contacts for capillary force-driven self-assembly," *Journal of Micromechanics and Microengineering*, vol.18, no., 10pp, 2008

[32] Stauth, S.; Parviz, B.;, "Self-assembled single-crystal silicon circuits on plastic," *PNAS*, Vol. 103, no. 38, 19 September 2006
URL: http://www.pnas.org/content/103/38/13922.full

[33] Drury, C. J.; Mutsaers, C. M. J.; Hart, C. M.; Matters, M.; de Leeuw, D. M.; , "Low-cost all-polymer integrated circuits," *Applied Physics Letters* , vol.73, no.1, pp.108-110, Jul 1998
doi: 10.1063/1.121783
URL: http://ieeexplore.ieee.org/stamp/stamp.jsp?tp=&arnumber=4898843&isnumber=4898804

[34] Lee, H.; Hong, S.; Yang, K.; Choi, K.; , "Fabrication of 100 nm metal lines on flexible plastic substrate using ultraviolet curing nanoimprint lithography," *Applied Physics Letters* , vol.88, no.14, pp.143112-143112-3, Apr 2006
doi: 10.1063/1.2193653
URL: http://ieeexplore.ieee.org/stamp/stamp.jsp?tp=&arnumber=4819388&isnumber=4819300

[35] Korivi, N.S.; Li Jiang; , "Metal Patterning on Polymers for Flexible Microsystems and Large-area Electronics," *System Theory, 2007. SSST '07. Thirty-Ninth Southeastern Symposium on* , vol., no., pp.181-185, 4-6 March 2007
doi: 10.1109/SSST.2007.352344
URL: http://ieeexplore.ieee.org/stamp/stamp.jsp?tp=&arnumber=4160830&isnumber=4160781

[36] Rajkowski, J.E.; Gerratt, A.P.; Schaler, E.W.; Bergbreiter, S.; , "A multi-material milli-robot prototyping process," *Intelligent Robots and Systems, 2009. IROS 2009. IEEE/RSJ International Conference on* , vol., no., pp.2777-2782, 10-15 Oct. 2009
doi: 10.1109/IROS.2009.5354068
URL: http://ieeexplore.ieee.org/stamp/stamp.jsp?tp=&arnumber=5354068&isnumber=5353884

[37] J. Rajkowski, "Rapid Polymer Prototyping for Applications in Low Cost and Robust Microrobots," master's thesis, Department of Mechanical Engineering, University of Maryland, College Park, MD, USA, 2010

[38] Wikipedia contributors, "Lux," *Wikipedia, The Free Encyclopedia*. Wikipedia, The Free Encyclopedia, 23 Mar 2010. Web. 16 Apr 2010
URL: http://en.wikipedia.org/wiki/Lux